



Fracturing and Energy Evolution of Rock Around Prefabricated Rectangular and Circular Tunnels Under Shearing Load: A Comparative Analysis

Jie Xin^{1,2} · Quan Jiang¹ · Shaojun Li¹ · Pengfei Chen^{1,2} · Herui Zhao^{1,2}

Received: 7 January 2023 / Accepted: 24 August 2023 / Published online: 15 September 2023
© The Author(s), under exclusive licence to Springer-Verlag GmbH Austria, part of Springer Nature 2023

Abstract

Mechanical behavior and energy evolution of rock around the tunnel are critical for evaluating the instability of geotechnical engineering. To reveal the influence of tunnel section shape on deformation, stress distribution, and fracturing mechanism of rock around the tunnel, a series of physical model shear tests for rock around prefabricated rectangular and circular tunnels were carried out, and corresponding fracturing and energy evolution analysis were also presented. In the shear test, the cracking evolution of rock around tunnel specimens was monitored and recorded by a high-speed camera and acoustic emission monitor to reveal the macro- and meso-fracture features. In addition, to examine the continuous-discontinuous shear process, four typical numerical models of rock around the tunnel were exploited to explore meso-mechanical behavior and fracturing mechanism. In light of the first law of thermodynamics, energy conversion process, damage characteristics and rockburst tendency of rock around tunnel specimens were investigated. The test results manifested that fracturing evolution, energy characteristic conversion, and micro-cracks evolution of rock around tunnel specimens generally were classified as four unified stages. In terms of fracturing evolution, rock around tunnel specimens experienced shearing compression stage (stage I), elastic stage (stage II) dominated by crack initiation, shearing fracture stage (stage III) dominated by crack propagation, coalescence and shear-induced rockburst, and shearing friction stage (stage IV). In the aspect of energy characteristic conversion, rock around tunnel specimens were mainly elastic deformation before peak shearing load, and the plastic deformation was relatively small. Partial dissipated strain energy acted on closing hole and crack initiation, and the rest was stored as elastic strain energy. After peak shearing load, the shear strength dropped rapidly, and a large amount of strain energy was converted into dissipated strain energy for crack propagation, coalescence and shear-induced rockburst. In the evolution of micro-cracks, the specimens underwent crack quiet period (stage I), crack initial increase stage (stage II), crack rapid increase stage (stage III), and crack stable stage (stage IV). Interestingly, the damage stress and rockburst tendency of rock around prefabricated rectangular tunnels were superior to those of rock around prefabricated circular tunnels, indicating that the bearing capacity of rock around prefabricated rectangular tunnels was superior to that of rock around prefabricated circular tunnels, related to the deviatoric stress distribution and confining pressure. In addition, a novel impact tendency index (S_p) was presented for evaluating shear-induced rockburst tendency, which carved the proportional relationship between elastic strain energy and dissipative strain energy at peak shearing load. The research results were conducive to recognize the fracturing mechanism of rock around a tunnel subjected to shear condition and provided a theoretical basis for the prevention and control of geotechnical engineering.

✉ Quan Jiang
qjiang@whrsm.ac.cn

Jie Xin
17203078017@stu.xust.edu.cn

Shaojun Li
sjli@whrsm.ac.cn

Pengfei Chen
chenpengfei21@mails.ucas.ac.cn

Herui Zhao
zhaoherui22@mails.ucas.ac.cn

¹ State Key Laboratory of Geomechanics and Geotechnical Engineering, Institute of Rock and Soil Mechanics, Chinese Academy of Sciences, Wuhan 430071, China

² University of Chinese Academy of Sciences, Beijing 100049, China

Highlights

- Shear characteristic, energy characteristic conversion and micro-cracks number evolution of rock around tunnel specimens generally were classified as four unified stages.
- Bearing capacity of rock around a prefabricated rectangular tunnel was superior to that of rock around a prefabricated circular tunnel, related to the deviatoric stress distribution and confining pressure.
- A novel damage variable was proposed to quantify the damage degree of rock
- A novel impact tendency index (Sp_{et}) was presented for evaluating the shear-induced rockburst tendency

Keywords Shear failure · Physical model · Fracturing mechanism · Energy conversion · Numerical calculation · Impact tendency index

List of Symbols

δ_h	Shear displacement
δ_h^t	Shear displacement at time t
δ_v	Normal displacement
δ_v^t	Normal displacement at time t
γ_p	Shear peak strain
μ	Particle friction coefficient
ν	Poisson ratio
ρ	Particle density
σ_n	Parallel-bond normal strengths
τ	Shear stress
τ_n	Parallel-bond shear strengths
τ_p	Shear strength
ΔU_d	Dissipative strain energy increment

Abbiations

AE	Acoustic emission
D	Damage variable
DEM	Discrete element method
E	Elastic modulus
E_c	Particle contact modulus
E_c'	Parallel bond modulus
E_t	Tensile modulus
G	Shear modulus
ISRM	International society for rock mechanics
k_n/k_s	Ratio of normal to shear stiffness of the particle
K_n'/k_s'	Ratio of normal to shear stiffness of parallel bond
PFC	Particle flow code
R_{max}/R_{min}	Ratio of maximum to minimum of radius
R_{min}	Minimum radius of the particle
Sp_{et}	Impact tendency index
U	Total energy
U_e	Elastic strain energy
U_d	Dissipated strain energy
U_n	Work of normal force
U_s	Work of shear force
V_p	Wave velocity

1 Introduction

Active demand for energy, resource, transportation, inevitably promotes the development of hydropower project, mining activity tunnel opening, and so on (Li et al. 2012; Whitworth et al. 2022; Yang et al. 2022). However, in the construction process of these projects, the instability shear problems of underground rock around tunnel are often encountered, such as shear large deformation, cracking, shear-induced rockburst (Jiang et al. 2017; Rahimi and Nygaard 2015; Zhang et al. 2020). For example, the shear zones (weak interlayer) of the arch-crown and side wall were vulnerable to extrusion failure in Baihetan hydropower station. In addition, rock fracture is gestated by the gradual development of internal micro-cracks subjected to shearing condition by energy release. In light of the first law of thermodynamics, rock fracture is accompanied by energy exchange and conversion, so the fracture mechanism was revealed with reference to energy (Zhao et al. 2020). However, the rock mass is a geological aggregate containing various types of discontinuities (such as holes) (Griffith 1921; Horii and Nemat 1985; Zhang et al. 2020; Zhu et al. 2022). Therefore, it is of great significance to investigate the fracturing and energy evolution of rock around tunnel with different shapes subjected to shear loading for controlling the instability of underground structures and preventing rock disasters.

The mechanical behavior and fracturing of rocks are the most challenging issues that are widely concerned by industry and academia (Bieniawski 1967; Brady and Rowell 1986; Xie et al. 1999). Currently, it is constructive to adopt a physical model test to investigate the mechanical behavior and fracturing of rock around tunnel subjected to compression conditions or excavation unloading, mainly focusing on prefabricated single crack (Huang et al. 2019; Liu et al. 2022b; Zhang et al. 2022), prefabricated double cracks (Xu et al. 2020b; Yang et al. 2016; Yue et al. 2020), prefabricated ubiquitous cracks (Cao et al. 2016a;

Sun 2021; Xu et al. 2020a), filled cracks (Liu et al. 2022c; Wu and Wong 2013; Zhang et al. 2021) and prefabricated holes (Huang et al. 2017; Jiang et al. 2019; Zhang et al. 2019a). For example, Liu et al. (2022b) carried out conventional triaxial compression tests on prefabricated single-crack specimens and found that the specimen was the most prone to initiation and there was large deformation when the crack inclination angle was 45°. Under uniaxial compression, Yang et al. (2016) investigated the strength characteristics and crack propagation behavior of specimens with two non-coplanar cracks caused by the ligament angle. It was found that the peak compressive strength of specimens depended on the ligament angle and the initiation, propagation and coalescence of cracks observed from the inner and outer ends of the prefabricated non-coplanar cracks. Zhang et al. (2021) presented a physical model test model with joints and holes subjected to uniaxial compression, the spalling phenomenon was observed in the upper right arch area. Huang et al. (2017) examined uniaxial compression tests on a physical model test model with three non-coplanar holes and determined three typical crack coalescence modes, i.e. shear, tension-shear mixed and tensile mode. It manifested from the literature that physical model test provided a valuable approach for reproducing and analyzing the mechanical behavior of rock. Meanwhile, combined with theoretical analysis and engineering practice, large deformation, spalling and rockburst caused by mechanics and fracture behavior of rock around tunnel under compression or excavation unloading were fully discussed. It laid a solid experimental and theoretical foundation for investigating the mechanical behavior and fracturing of rock around the tunnel. However, stress-structural disasters (such as fracture behavior, rockburst) were common in deep hard rock engineering, but mechanical behavior and fracturing of rock around the tunnel subjected to shear loading were rarely discussed and exploited.

In addition, there were gaps that the initiation, propagation and coalescence of cracks cannot be accurately quantified in laboratory tests. With the development of numerical methods, a variety of numerical calculation software have been applied to analyze the mechanical behavior and fracture, such as particle flow code [PFC^{2D} (Jiang et al. 2022), PFC^{3D} (Fan et al. 2018)], rock failure process analysis (RFPA) (Wong and Lin 2015), Cellular Automata (Pan et al. 2009), and X finite element (Colombo and Massin 2011). Among them, in the light of the discrete element method (DEM) (Xin et al. 2024), particle flow code (PFC) presented an excellent advantage in capturing crack behavior, and obtained crack initiation stress, damage stress, crack number and stress–strain curve. And, it was easy to record the crack propagation path and distinguish the type of cracks. Therefore, the numerical simulation (PFC)

was an effective auxiliary tool to investigate the fracture behavior of rock around tunnel.

The nature of stress-structure failure (shear large deformation, rockburst) was energy exchange and conversion of rock in deep hard rock engineering, and research mainly concentrated upon the energy problem of rock under compression condition (Bratov and Petrov 2007; Cornetti et al. 2006; Fedotova et al. 2017; Feng et al. 2019; Ferro 2006; Yang et al. 2023; Zhang et al. 2019b, 2019c; Zhao et al. 2020; Zhu et al. 2023). Zhao et al. (2020) investigated that in the plastic failure stage, dispersed energy rose sharply, the elastic energy was released rapidly, and rockburst was accompanied by fragmentation subjected to uniaxial compression. In the true triaxial state, Feng et al. (2019) found that the variation of strain energy before the peak was basically similar, while the variation after the peak was quite non-uniform, especially when the intermediate principal stress was large. Zhang et al. (2019c) examined an inverse relationship between elastic strain-energy and dissipative strain energy subjected to true triaxial loading. The above literatures provide experimental and theoretical approaches for the study of rock energy exchange and conversion, but they mainly converged on the compression condition, while there were few studies on energy exchange and conversion of rock around tunnel subjected to shear loading.

Thus, to reveal the influence of tunnel section shape on deformation, stress distribution, and fracturing mechanism of rock around the tunnel, rock around prefabricated rectangular and circular tunnels were prepared, and physical models shear tests of specimens were carried out by servo shear test system. In the process of the shear test, the cracking evolution was monitored and recorded by high-speed camera and acoustic emission monitor to reveal its macro- and meso-fracture characteristics. To in-depth understand the mechanical behavior and fracturing of rock around the tunnel and make up for the gaps of the physical model shear test, PFC^{2D} was adopted to establish four typical numerical models of rock around the tunnel with tunnel section shapes, and the continuous-discontinuous shearing process was thoroughly exploited. In light of the first law of thermodynamics, the energy conversion process and rockburst tendency of rock around the tunnel were investigated.

2 Materials and Methods

2.1 Experimental Materials

The petrography and microstructure of sandstone are investigated by petrographic images and electron microscope scanning images, as shown in Fig. 1. The petrographic evidence implied that sandstone was mainly composed of quartz

(60%), and the mineral particle size was 0.06–0.50 mm (Fig. 1a). The rock belonged to fine-grained feldspar quartz sandstone with fine-grained structure and massive structure (Wu et al. 2021). In combination with Fig. 1a, the basic structural units of exfoliated rock were mainly irregular block structures and randomly distributed. The block structures of basic structural units were usually characterized by edge-plane, edge-edge and plane-shape (Fig. 1b) (Ruan et al. 2023). In line with the method of the International Rock Mechanics (ISRM) (Aydin 2009), the physical mechanics parameters of rock were tested and results were shown in Table 1.

2.2 Experimental Scheme

The preparation of rock around tunnel specimen was shown in Fig. 2. In conformity with the method proposed by ISRM (Aydin 2009), rock around prefabricated rectangular and circular tunnels are manufactured, and the dimensions of the test sample is cuboids (i.e., $L \times W \times H = 300 \times 200 \times 200$ mm), and the tunnel is also cuboid (i.e., $L \times W \times H = 60 \times 60 \times 200$ mm) and cylinder (i.e., $\varphi \times H = 50 \times 200$ mm). This ensured that stress distribution was uniform in rock specimen. The reason for choosing two shapes, on the one hand, was that the section shape was often adopted in practical engineering, which had a pivotal impact on the instability and failure characteristics of rock around the tunnel. On the other hand, the geometric shape was basically symmetrically, eliminated the influence of other variables on the preliminary study. The shear tests of rock around prefabricated rectangular and circular tunnels were carried out with the constant normal loads, respectively, at the shear rate of 0.005 mm/s (AC10520942 2008). The test scheme is shown in Table 2.

2.3 Experimental Set-Up

The high-stress loading and unloading servo shear test system of the rock structural plane is adopted to carry out a shear test. The servo-driven shear test device was equipped with an observation window to observe the shearing process. The system automatically recorded the loading and deformation information. In the shearing process, two high-speed cameras were observed external crack evolution and internal failure of specimens, respectively. In addition, two acoustic emission (AE) sensors were installed on both sides of the specimen, and recorded the AE events in the shearing process. To avoid possible environmental noise, the detection threshold was set to 45 db (Wu et al. 2019), and test schematic diagram was shown in Fig. 3.

3 Experiment Results and Analysis

To reveal the mechanical behavior and fracturing of rock around tunnel specimens subjected to shear loading, the compression-shear test of specimens were carried out by a servo shear test system. With the aid of high-speed cameras, acoustic emission monitor and the first law of thermodynamics, mechanical behavior and energy characteristics were recorded and observed, including shear characteristic curves, crack behavior and energy characteristic conversion curves.

The primary reasons for the division of four typical stages subjected to shear loading are as follows: in the typical stage, the difference in the internal mechanism of rock gave rise to the variation in mechanical behavior and energy evolution. And in the light of phenomenological theory and the real-time state of rock rather than the shearing characteristics curves.

3.1 Shearing Characteristic Curve and Typical Stage

Shear stress (τ), shear displacement (δ_h), and normal displacement (δ_v) rock around the tunnel were recorded subjected to shear loading. With reference to the shear characteristic curve (Fig. 4), the τ - δ_h and δ_v - δ_h characteristic curves of rock around prefabricated rectangular and circular tunnels displayed similar mechanical behaviors. On the ground of the slope, inflection point and failure process of the shear characteristic curve, four typical stages were divided: shear compaction (stage I), linear elasticity (stage II), shearing fracturing (stage III) and shearing friction (stage IV).

Shearing compaction stage (stage I): from the origin point to point A, the shearing load increased non-linearly with the increment of displacement. The primary open cracks and holes closed, resulting in slight shear contraction ($\delta_v < 0$), consistent with the research phenomenon of Yang et al. (2022). Moreover, no crack initiation in stage I.

Linear elasticity stage (stage II): From point A to point B, the characteristic curves (τ - δ_h and δ_v - δ_h) demonstrated a positive correlation, while δ_v - δ_h curves carved a trend of dilatancy. In addition, there were micro-cracks inside the specimens, but no obvious failure phenomenon was observed on the surface of the specimens.

Shearing fracture stage (stage III): corresponding to the point (B–C), the characteristic curve (τ - δ_h) first increased convex and then dropped suddenly, while the characteristic curve (δ_v - δ_h) exhibited obvious dilatancy feature. And the secondary crack initiated and propagated with the increment of deformation. At the peak shearing load, the secondary crack coalesced with the prefabricated tunnel and formed a macroscopic fracture surface. Then, the shearing load dropped sharply, indicating that the specimen revealed brittle failure.

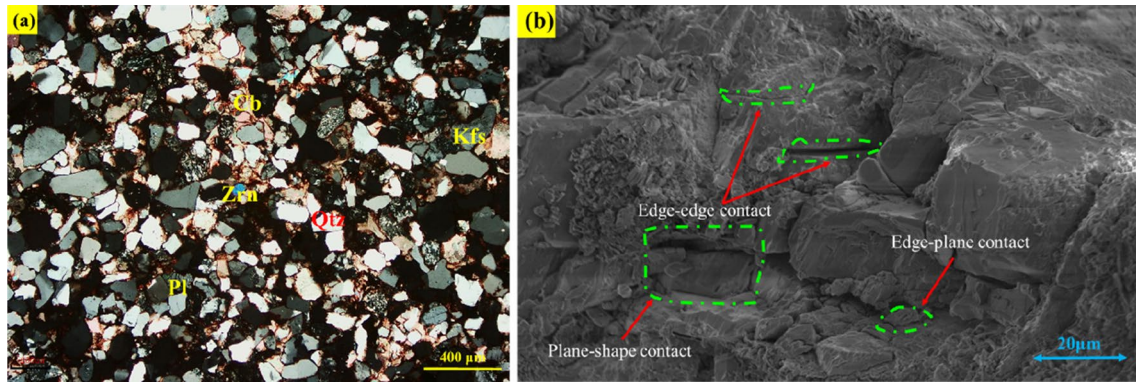
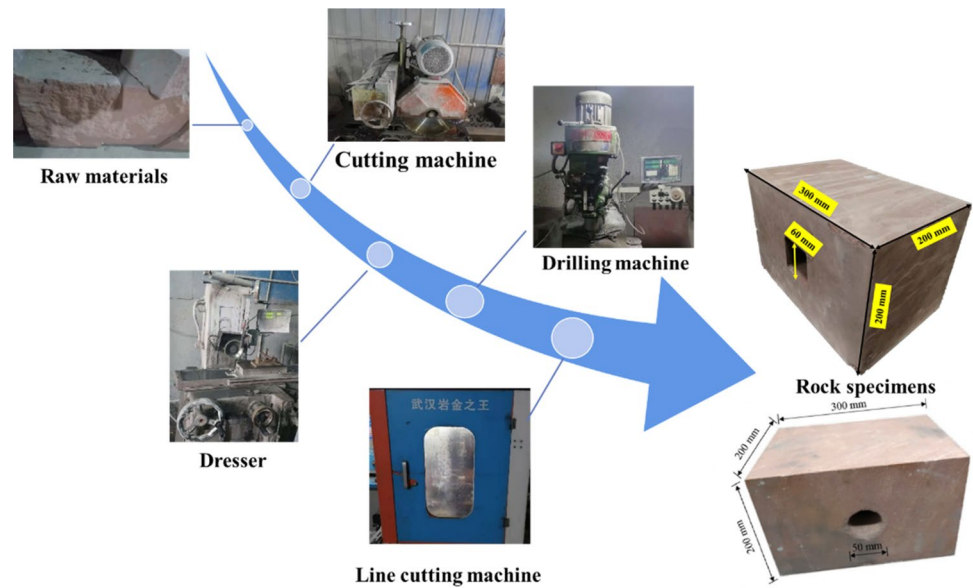


Fig. 1 Petrographic analysis of sandstone: a plane-polarized light, b scanning electron microscope

Table 1 Basic mechanical parameters of sandstone

Colour	σ_c , MPa	E_c , GPa	σ_t , MPa	E_t , GPa	ν	V_p , (km/h)
Red	45.21	10.90	1.16	4.40	0.24	3.70

Fig. 2 Specimen processing flow chart



Shearing friction stage (stage IV): after point C, characteristic curve ($\tau-\delta_h$) was basically horizontal, and the characteristic curve ($\delta_v-\delta_h$) presented a tendency shear contraction. And the specimens was in the ideal plastic shear friction state. Moreover, the mechanical behavior of rock' joint surface gradually changed from the dominant state of cohesion and internal friction angle to that of dispersed

rock blocks, rock particles and rock debris, consistent with the research phenomenon of Jiang et al. (2022).

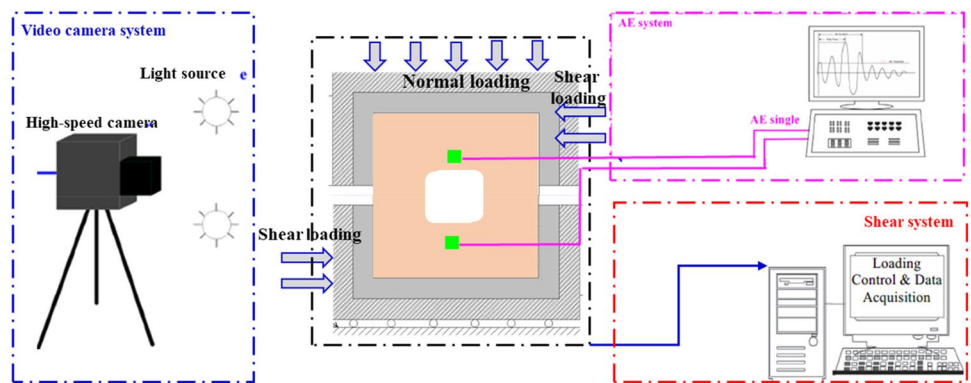
3.2 Strength and Deformation Characteristics

According to the definition and classification criteria of rock brittleness index (Wang et al. 2021; Liu et al. 2022a), in

Table 2 Loading scheme of rock around tunnel

Tunnel model	Loading mode	Normal stress , MPa	Loading rate, mm/s
Rock around prefabricated rectangular tunnel		2.0,3.5,5.0	0.005
Rock around prefabricated circular tunnel		2.0,4.0,5.0	0.005

Fig. 3 Experimental schematic diagram



this study, the brittleness index (σ_c/σ_t) of sandstone is 38.96, belonging to brittle rock. In addition, the characteristic curve ($\tau-\delta_h$) of rock around tunnel specimens presented stress reduction phenomenon, mainly caused by the initiation or propagation of cracks. Combined with the mechanical parameters of the rock around tunnel specimens in Table 3, the influence of normal stress and tunnel section shape on the shear strength (τ_p) was analyzed and discussed, and the parameters (G and γ_p) of deformation characteristics were given. The mechanical parameters were defined as follows: τ_p , G and γ_p were defined as shear strength, shear modulus and shear peak strain. Specifically, the shear modulus of rock is calculated by evaluating the ratio of shear stress and shear strain in linear elastic (stage II).

Figure 4 and Table 3 manifested that the normal stress exhibited a significant effect on the mechanical parameters of rock around prefabricated rectangular and circular tunnels. As the increment of normal stress, the τ_p of rock around prefabricated rectangular and circular tunnels increased significantly, but the shear strength of rock around prefabricated circular tunnel increased lower than that of rock around prefabricated rectangular tunnel. Specifically, when increment of normal stress (2.0–5.0 MPa), the τ_p of rock around prefabricated circular tunnel increased from 5.24 to 8.63 MPa

(increased by 40.4%), while that of rock around prefabricated rectangular tunnel increased from 5.25 to 8.74 MPa (increased by 37.8%). This may be because the higher normal stress made the distance between the rock particles closer, enhancing the cohesion of the rock (Jaeger 1979).

Compared with normal stress, the influence of tunnel section shape on shear strength was relatively small. Shear strength of rock around prefabricated rectangular and circular tunnels was 5.24–8.63 MPa and 5.25–8.74 MPa, respectively, when the normal stress was 2.0–5.0 MPa, but the shear strength of rock around prefabricated rectangular tunnel was greater than that of rock around the prefabricated circular tunnel, regardless of normal stress. This was different from the view that the bearing capacity of the circular tunnel section was higher. This fact can be explained as that the structural effect can offset the deterioration effect of prefabricated holes on rock to a certain extent (Haijian et al. 2014; Zhu et al. 2019). Meanwhile, the detailed mechanism analysis was given in Sect. 4.2. Consistent with this test, due to the existence of circular and rectangular tunnels, the effective load area of the specimen was reduced to 83.3% and 80%, respectively, in line with the structural effect conditions of rock around the tunnel.

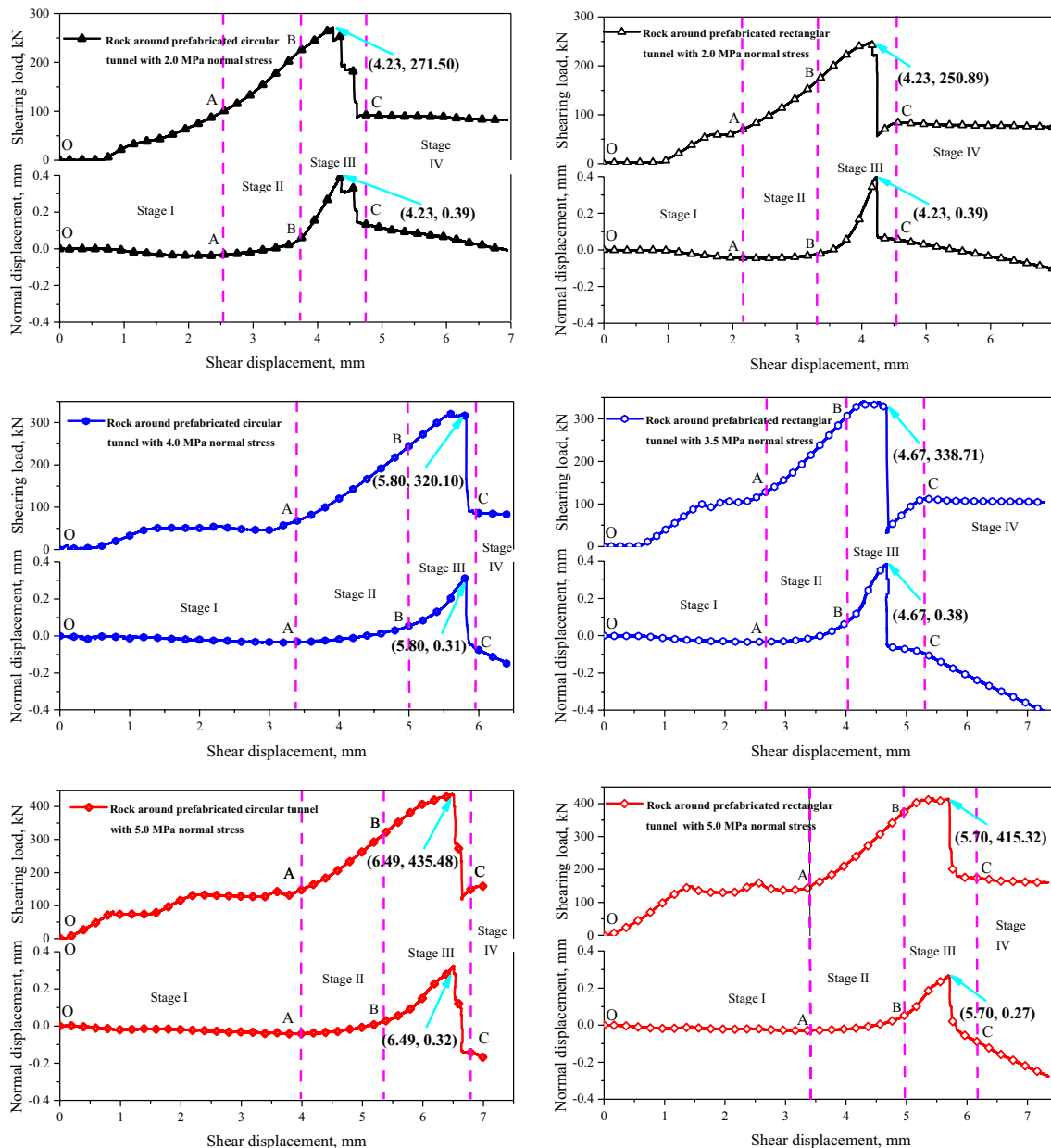


Fig. 4 Shearing load—deformation, dilatancy curve and typical stage division of rock around tunnel specimens

3.3 Acoustic Emission and Fracture Characteristics

To explore the influence of tunnel section shape on acoustic emission and fracturing, taking two typical section shapes of rock around prefabricated circular tunnel with 5.0 MPa normal stress and rock around prefabricated rectangular tunnel with 5.0 MPa normal stress as examples for discussion and analysis. The high-speed camera and acoustic emission monitor were adopted to record and observe internal failure phenomena (crack initiation, buckling and shear-induced rockburst), the external crack evolution (crack initiation, propagation and coalescence), and acoustic emission

characteristics subjected to compressive-shear conditions, to better understand mechanical behavior and fracturing (Cao et al. 2016b; Debecker and Vervoort 2013; Yang et al. 2016). The AE counts, cumulative AE counts, and shearing load-time curves were shown in Fig. 5a and 6a. In conformity with the characteristic curve in Sect. 3.1, it can be divided into four typical stages (different colors in the area), and the typical behavior of AE and fracturing evolution of the specimen successively, corresponded to the points (a–e). In addition, Fig. 5a₁–e₁, Fig. 6a₁–e₁ and Fig. 5a₂–e₂, Fig. 6a₂–e₂ described the typical fracture behavior inside the tunnel and the evolution of external cracks. Where, point (a, b) for stage

I–II typical behavior, point (c, d) for stage III fracturing; point e for stage IV typical feature.

Shearing compaction stage (stage I): The fracture behavior of rock around prefabricated rectangular and circular tunnels was analogous. When the specimens were loaded to point a (about $\tau = 0.2\tau_p$), from the internal fracture process (Fig. 5a₁, Fig. 6a₁) and the external crack evolution (Fig. 5a₂, Fig. 6a₂) of the specimens, no obvious damage phenomenon was observed and the specimen was in a complete state, but the stress reduction occurred. Meanwhile, some AE events were detected (Fig. 5a), but the cumulative AE counts remained almost constant with the increase of deformation. This was because the closure of primary pores and cracks in samples would not lead to the release of strong strain energy, which was consistent with the results of Xiong et al. (2011).

Linear elasticity stage (stage II): the fracturing behavior of rock around prefabricated rectangular and circular tunnels was significantly different. For rock around the prefabricated rectangular tunnel, as the shear deformation increased, the specimen was loaded to point b (about $\tau = 0.9\tau_p$). In terms of the internal fracture process, small particles fell off at the upper right shoulder angle, and occasionally there were ejection of small particles, accompanied by buckling (Fig. 5b₁). This indicated that the upper right shoulder angle was first damaged, associated with crack initiation. In the aspect of the evolution of the external cracks, two main macro- tensile cracks (1^a and 1^b) initiation at the upper left shoulder angle and the lower right shoulder angle. Meanwhile, the main macro- shear cracks (2^a) was coalesced and 1^b (Fig. 5b₂) and propagated along about 30° with the loading direction. Meanwhile, a large AE event was monitored, associated with the proliferation in AE cumulative ringing counts. This echoed with the elastic–plastic conversion point. For rock around the prefabricated circular tunnel, the shear stress corresponding to the elastic–plastic transition point was significantly reduced, different from the rock around prefabricated rectangular tunnel, which was confirmed by the results of Chen et al. (2021). When the specimen was loaded to the point b (about $\tau = 0.56\tau_p$), In the aspect of the

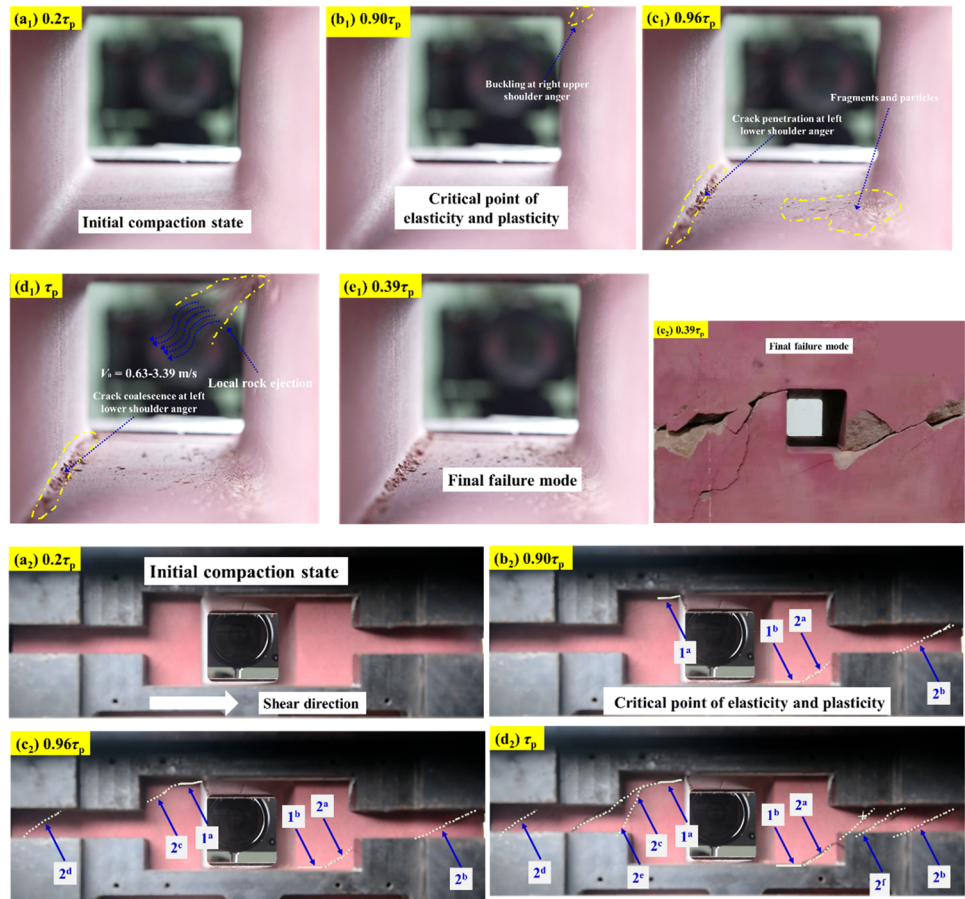
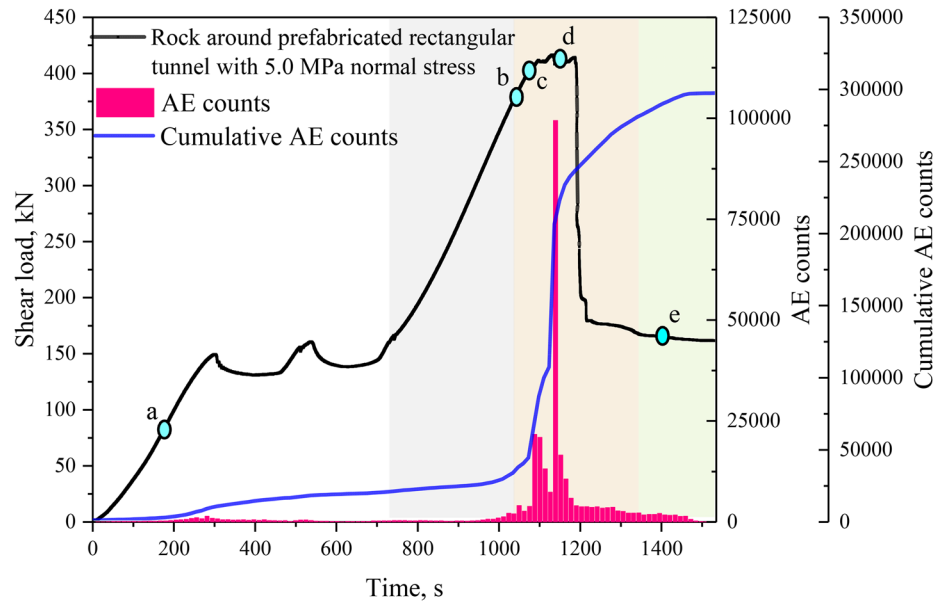
internal fracture process, small particle ejection occurred at the bottom of the tunnel, but the ejection speed was very small, accompanied by buckling (Fig. 6b₁), echoed by the AE events. This manifested that there was a fracture behavior at the bottom of tunnel, different from the failure position of rock around the prefabricated rectangular tunnel. In terms of the evolution of the external crack, the macro quasi-main shear crack (1^a) initiated and propagated at the bottom (Fig. 6b₂), with a tendency to propagate the tunnel bottom to the right middle end of the specimen.

Shearing fracture stage (stage III): in terms of the internal fracturing of rock around prefabricated rectangular tunnel, with an increment of shear deformation, loaded to point c (about $\tau = 0.96\tau_p$), cracks appeared at the lower left shoulder angle (Fig. 5c₁). About 3 s later, in the upper right shoulder angle, significant cracks occurred with the ejection of small particles. As the shear deformation increased, the specimen was loaded to point d (about $\tau = \tau_p$), and the crack propagated rapidly at the lower left shoulder angle, and then the cracks obviously coalesced the tunnel axis. And, the ejection of fragments occurred at the right upper shoulder angle, and then shear-induced rockburst broke out (Fig. 5d₁), harmony with in-situ the fragments (1–10 m/s) (Ortlepp and Stacey 1994). The shear-induced rockburst caused the shear stress to decrease significantly, from τ_p to $0.39\tau_p$. In the aspect of the evolution of external cracks, when the specimen was loaded to point c (about $\tau = 0.96\tau_p$), the tensile-shear cracks (1^b–2^a–2^b) and the tensile-shear cracks (1^a–2^c–2^d) propagated steadily and gradually formed shear bands (Fig. 5c₂). With the increment of shear deformation, the specimen was loaded to d point (about $\tau = \tau_p$), cracks (1^b–2^a–2^b–2^f) coalesced the right middle end of the specimen with the right lower shoulder angle and cracks (1^a–2^c–2^d–2^e) coalesced the left middle end of the specimen with the left upper shoulder angle (Fig. 5(d₂)). And, the largest acoustic emission event was observed (Fig. 5d); the AE cumulative ringing counts manifested an exponential proliferation. In the aspect of the internal fracture process of rock around prefabricated circular tunnel specimen, the specimen was loaded to point c (about $\tau = 0.93\tau_p$) and point d (about $\tau = \tau_p$), obvious cracks

Table 3 Results summary of mechanics characteristic parameters

Sample	Shear stress (τ_p), MPa	Shear modulus (G), MPa	Peak strain, (γ_p) %
Rock around prefabricated circular tunnel with 2.0 MPa normal stress	5.24	101.53	4.23
Rock around prefabricated rectangular tunnel with 2.0 MPa normal stress	5.25	103.52	4.14
Rock around prefabricated circular tunnel with 4.0 MPa normal stress	6.51	80.58	5.59
Rock around prefabricated rectangular tunnel with 3.5 MPa normal stress	6.87	127.53	4.29
Rock around prefabricated circular tunnel with 5.0 MPa normal stress	8.63	125.21	6.48
Rock around prefabricated rectangular tunnel with 5.0 MPa normal stress	8.74	101.99	5.38

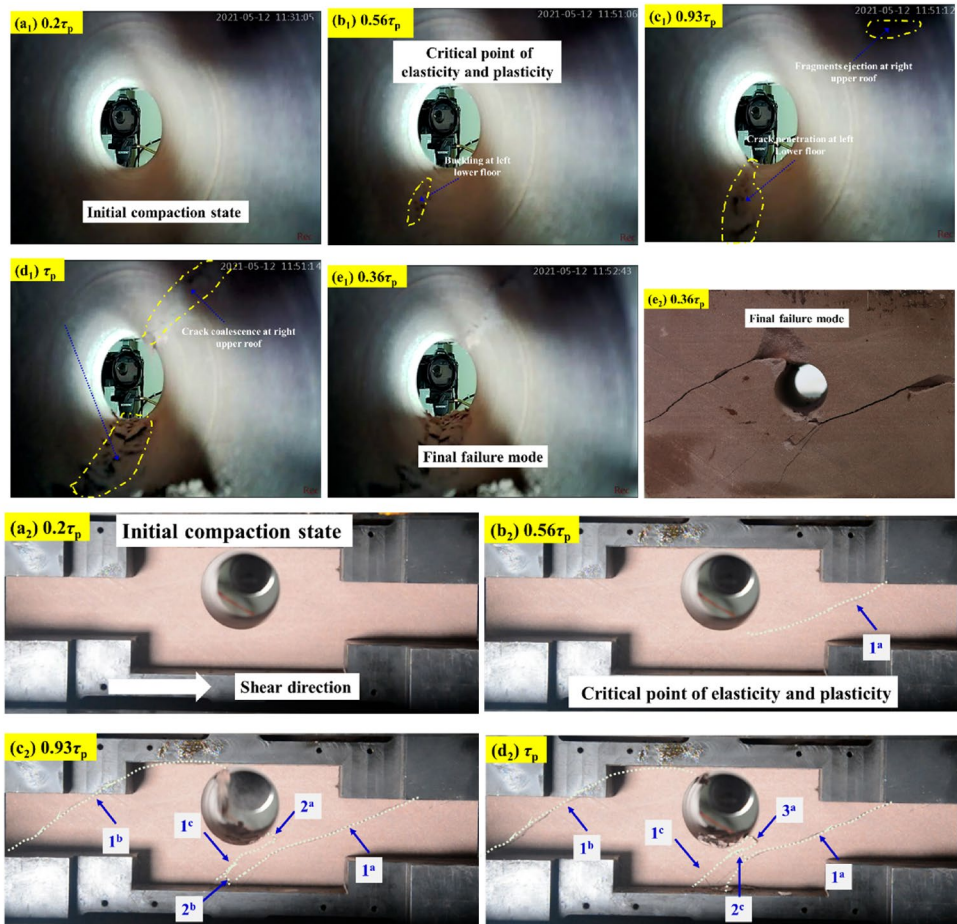
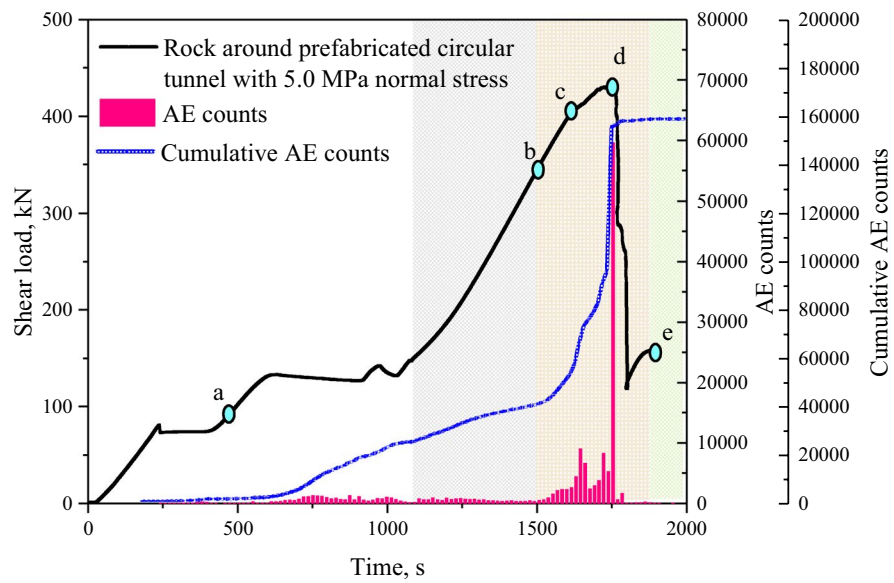
Fig. 5 Acoustic emission and fracture characteristics: rock around prefabricated rectangular tunnel with 5.0 MPa normal stress



appeared at the tunnel bottom and vault, accompanied by small particles ejection (Fig. 6c₁). After that, the cracks obviously coalesced the tunnel axis. Meanwhile, the shear-induced rockburst occurred, accompanied by the ejection of debris at the tunnel bottom. There was a maximum ejection velocity (about 2.51 m/s), leading to a significant reduction

in stress ($\tau_p - 0.36\tau_p$). In terms of the external crack evolution, with an increment of shear deformation, loaded to point c (about $\tau = 0.93\tau_p$) and point d (about $\tau = \tau_p$), two macrocracks were initiated at the vault and bottom of the tunnel. The tensile-shear crack (1^b) initiated at the vault of the tunnel and propagated about 30° along the loading direction,

Fig. 6 Acoustic emission and fracture characteristics: rock around prefabricated circular tunnel with 5.0 MPa normal stress



coalescing the vault with the left middle end of the specimen (Fig. 6c₂). Cracks (1^a–2^a–2^b–2^c–3^a) rapidly formed macro-shear crack bands at the bottom of tunnel, coalescing them with the right middle end (Fig. 6d₂).

Shearing friction stage (stage IV): The fracture behavior of rock around prefabricated rectangular and circular tunnels was similar. Corresponding to Sect. 3.1, with the increment of deformation, the shear stress continued to drop, entering stage IV, but the residual stress was about 0.2–0.36τ_p. With

increment of shear deformation, loaded to point e, the shear-dominated mixed failure was formed (Fig. 5e₂, Fig. 6e₂).

Fracturing process of rock around the tunnel under other normal stresses was similar to that with 5.0 MPa normal stress. The test results manifested that rock around the tunnel experienced shearing compression stage (stage I), linear elasticity stage (stage II) dominated by crack initiation, shearing fracture stage (stage III) dominated by crack propagation, coalescence and shear-induced rockburst, and shearing friction stage (stage IV). It was noteworthy that rock around prefabricated circular tunnel focused on the vault and bottom of the tunnel, while the rock around prefabricated rectangular tunnel paid attention to the upper right shoulder angle and the lower left shoulder angle. Interestingly, the damage stress and rockburst tendency of rock around prefabricated rectangular tunnel were superior to those of rock around prefabricated circular tunnel, related to the deviatoric stress distribution and confining pressure of rock around the tunnel.

3.4 Failure Mode

Failure mode is a critical method to understand the cracking mechanism of rock. To reveal the influence of section shapes and normal stresses, the failure modes of rock around prefabricated rectangular and circular tunnels were investigated in-depth. On the ground of previous research results of crack identification (Fan et al. 2022), it was found that tensile cracks, shear cracks, mixed cracks and secondary cracks appeared in the rock around tunnel.

According to the shear failure features in Table 4, the failure mode was determined, in which the green line was the main crack and the brown area was the spalling area. In rock around prefabricated rectangular and circular tunnels specimens, new cracks always initiate on the surface of rock around the tunnel and propagate in the inclined loading direction, eventually leading to the failure. It can be seen from Table 4 that the failure modes of rock around prefabricated rectangular and circular tunnels specimens were analogous. The typical shear failure characteristics of rock around prefabricated rectangular and circular tunnels specimens were divided into upper and lower parts by crack ②, showing shear-dominated mixed failure mode with a quasi-centered symmetry. But normal stress revealed considerable effect on shear failure mode. Specifically, rock around prefabricated rectangular tunnel with 2.0 MPa normal stress exhibited two cracks ② and local area rock spalling, while rock around a prefabricated rectangular tunnel with 5.0 MPa normal stress presented more complex shear failure modes, with the presence of secondary cracks (cracks ③, cracks ④, and cracks ⑥). While rock around prefabricated circular tunnel with 2.0 MPa normal stress, there were the presence of secondary cracks (crack

④ and crack ⑤). Rock around prefabricated circular tunnel with 5.0 MPa normal stress depicted a more complex failure mode. In short, the higher the normal stress, the more complicated failure modes.

3.5 Energy Evolution Characteristics

Rock fracturing is mainly caused by crack propagation and coalescence, and energy dissipation is the key factor (Han et al. 2020; Zhou et al. 2020). In the shearing process, the accumulation, dissipation and release of energy follow the first law of thermodynamics (Huang and Li 2014). This is because when the quasi-static load is loaded, the thermal energy, kinetic energy and acoustic energy generated by loading, are negligible compared with the work done (Wang and Yan 2012). The accumulation of energy is the input of mechanical energy into the system by external work, and the dissipation of energy is to convert a portion of mechanical energy into heat energy and dissipate through the interactions between particles. Both processes adhere to the first law of thermodynamics (Nakatani 2001). Thus, the energy can be expressed by elastic strain energy (U_e) and dissipated strain energy (U_d). The relationship can be expressed as

$$U = U_e + U_d, \quad (1)$$

where U , U_e and U_d are total energy, elastic strain energy and dissipated strain energy, respectively.

$$\begin{cases} U = U_n + U_s \\ U_n = \int_0^{\delta_v^t} F_n d\delta_v \\ U_s = \int_0^{\delta_h^t} F_s d\delta_h \end{cases}, \quad (2)$$

where U_n and U_s are the work of normal force and shear force. δ_v is normal displacement, δ_h is shear displacement, δ_v^t is normal displacement at time t , δ_h^t is shear displacement at time t , F_n is normal force, F_s is shear force.

$$U_e = \frac{1}{2} \int_0^{\delta_h^t} \frac{F_s^2}{GA} d\delta_h, \quad (3)$$

where G and A are the initial shear modulus and cross-sectional area, respectively. Wang and cui (2018) proposed that the unloading elastic modulus was close to the initial elastic modulus. To facilitate the calculation, the initial shear modulus instead of the unloading elastic modulus was adopted.

With reference to Eq. (3), the energy characteristic conversion process curves of U , U_e and U_d of rock around prefabricated rectangular and circular tunnels with normal stresses were calculated, as shown in Fig. 7. By exploring characteristic curves, it was found that the energy evolution

Table 4 Failure modes of specimens

Specimen failure diagram	Failure mode	Annotation
	Shear-dominated mixed failure	① is spalling area; ② is quasi-tensile-shear crack; ③ is oblique secondary crack; ④ is quasi-coplanar secondary crack; ⑤ is quasi-tensile-shear secondary crack; ⑥ is quasi-oblique secondary crack;
	Shear-dominated mixed failure	① is spalling area; ② is quasi-tensile-shear crack; ③ is oblique secondary crack; ④ is quasi-coplanar secondary crack; ⑤ is quasi-tensile-shear secondary crack; ⑥ is quasi-oblique secondary crack;
	Shear-dominated mixed failure	① is spalling area; ② is quasi-tensile-shear crack; ③ is oblique secondary crack; ④ is quasi-coplanar secondary crack; ⑤ is quasi-tensile-shear secondary crack; ⑥ is quasi-oblique secondary crack;
	Shear-dominated mixed failure	① is spalling area; ② is quasi-tensile-shear crack; ③ is oblique secondary crack; ④ is quasi-coplanar secondary crack; ⑤ is quasi-tensile-shear secondary crack; ⑥ is quasi-oblique secondary crack;

of rock around prefabricated rectangular and circular tunnels revealed similar characteristics. The relationship between energy conversion and shearing load-deformation in four stages was discussed and analyzed in detail.

Shearing compaction stage (stage I): as shearing load was at a low level, the strain energy, elastic strain energy and dissipation strain energy absorbed by rock around prefabricated rectangular and circular tunnels were small, the characteristic curve was gentle, and the difference between U and U_d was minor. This manifested that the absorbed U was mainly converted into U_d , mainly consumed by the compaction of primary fracture and pores. The increase of shear deformation was faster than the increment of shearing load, and the

curve was concave, aligned with the behavior of rock around the tunnel in Sects. 3.1 and 3.3

Linear elasticity stage (stage II): three forms of energy absorbed by rock around prefabricated rectangular and circular tunnels gradually increased with the increment of shearing load. The total strain energy absorbed was mainly stored in the form of elastic energy. Although the dissipated energy of the specimens increased during the loading process, the slope of the dissipated energy curve was smaller than that of the remaining two.

Shearing fracture stage (stage III): as the loading continued, the total strain energy absorbed by rock around prefabricated rectangular and circular tunnels still increased, but the dissipation energy proliferated sharply. This process

aggravated the internal damage of the specimen, resulting in ultimate failure. After that, the elastic strain energy was released rapidly, and the dissipation energy increased rapidly. The energy release led to the rapid propagation and coalescence of macro-cracks, breaking the rock into independent fragments and causing damage. When the released energy was large, the broken rock would eject outwards, resulting in a shear-induced rockburst (Fig. 5d₁) in Sect. 3.3.

Shearing friction stage (stage IV): the elastic strain energy of rock around prefabricated rectangular and circular tunnels was basically in the residual state, and there was no tendency of energy release.

On the ground of the analysis, the rock around the tunnel were mainly elastic deformation before the peak shear strength, and the plastic deformation was relatively small. Partial dissipated strain energy was applied to closed hole and crack initiation, and the rest was stored as elastic strain energy. After the peak shear strength, the shear strength of the specimens dropped rapidly, and a large amount of strain energy was converted into dissipated strain energy for crack propagation, coalescence and shear-induced rockburst. The larger the elastic energy release rate was, the more fragments triggered by rock breaking, and the higher the rockburst tendency of rock around the tunnel.

4 Numerical Back-Analysis and Mechanism Interpretation

To in-depth reveal the cracking mechanism of rock around tunnel, the compression-shear test numerical model was set up by DEM. With the aid of self-compiled monitoring programs, mechanical behaviors that cannot be observed in laboratory tests, including stress distribution, crack propagation and displacement fields, can be visualized and quantified.

4.1 Numerical Model and Parameter Calibration

In the light of DEM, PFC provides a scientific tool for studying the fracture mechanism of rock around tunnel, especially in simulating crack propagation and stress field distribution (Wang and Yan 2023; Wang et al. 2023a, b). In PFC, parallel bond model (PBM) has been shown to reproduce the mechanical response of rock (Li et al. 2018; Potyondy and Cundall 2004; Wang et al. 2003). Thus, the PBM was adopted to explore the fracture mechanism of rock around the tunnel.

Figure 8 displays the shear numerical model established by PFC^{2D}, with uniform particle size distribution. The particle size distribution was 0.25–2.5 mm, and the size of the model was consistent with that of the physical model test. The numerical model consisted of more than 20,000

particles and 52,000 contact points, and contact between the particles adopted PBM. The rock around the tunnel model was generated after removing the ball in a specific area (Fig. 8). The shear deformation was controlled by displacement, and the loading rate (0.005 mm/s) was in a quasi-static loading state. It was well known that the reasonable selection of PFC meso-parameters was an effective way of achieving ideal simulation results. The trial and error method was adopted until the shear characteristics of the numerical model were consistent with the test results. The meso-parameters of PFC calibrated by the numerical model test were shown in Table 5. Based on the calibrated meso-parameters in Table 5, rock around prefabricated rectangular and circular tunnels numerical shear tests were carried out. Figure 9 and Table 6 were the mechanical indexes and failure modes, respectively. The numerical shearing load-deformation curve and failure mode were consistent with the test results. The characteristic parameters in Fig. 9 were summarized in Table 7. It was found that the error of the characteristic parameters between the test and the simulation was within 5%, which strongly verified the reliability of the numerical simulation. The above errors were explained as follows: first, two-dimensional analysis cannot accurately simulate three-dimensional tested specimens (Yang et al. 2016). Secondly, it was related to rock heterogeneity. Thirdly, the numerical model adopted a circular ball, without considering the shape and angle of the particles, different from the physical particle.

4.2 Crack Behavior and Stress Field Distribution

Laboratory shear tests of rock around prefabricated rectangular and circular tunnels were carried out, and the fracturing was investigated in detail in Sect. 3. Considering the complexity of the shear test, no shear test was conducted on other section shape of specimens. Crack initiation, propagation, and coalescence subjected to shear loading can be reproduced by numerical calculation. The reliability of rock around prefabricated rectangular tunnel with 5.0 MPa and rock around prefabricated circular tunnel with 5.0 MPa was verified in Sect. 4.1. Therefore, numerical models with tunnel section shapes were established by PFC^{2D} to comprehensively investigate the meso-fracture behavior.

According to the typical stages of shear characteristic curve of physical model and cracking behavior of the numerical model, the characteristic curves of the numerical model with section shapes were organized into four typical stages, as shown in Fig. 10. With reference to typical characteristics of the shear stress-displacement and crack-num curves in Fig. 10, Table 8 depicted the crack initiation, propagation and coalescence of rock around tunnel models with section shapes simulated by PFC^{2D} subjected to shear loading. The failure process corresponded to the points (a–d) on the shear

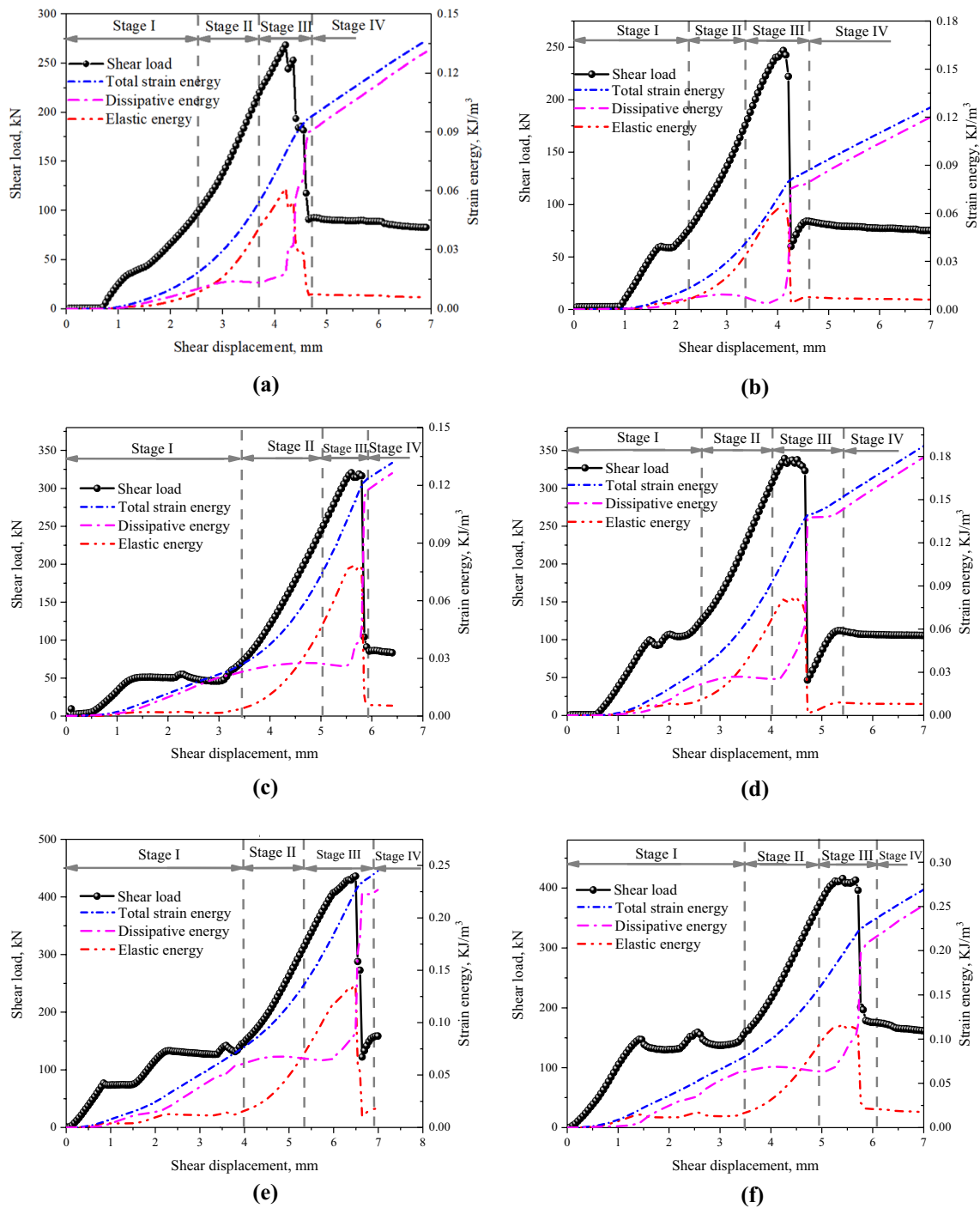


Fig. 7 Shear characteristic curve and energy conversion curve: **a** rock around prefabricated rectangular tunnel with 2.0 MPa normal stress, **b** rock around prefabricated circular tunnel with 2.0 MPa normal stress, **c** rock around prefabricated rectangular tunnel with 3.5 MPa

normal stress, **d** rock around prefabricated circular tunnel with 4.0 MPa normal stress, **e** rock around prefabricated rectangular tunnel with 5.0 MPa normal stress, **f** rock around prefabricated circular tunnel with 5.0 MPa normal stress

Fig. 8 Numerical model established by PFC^{2D}

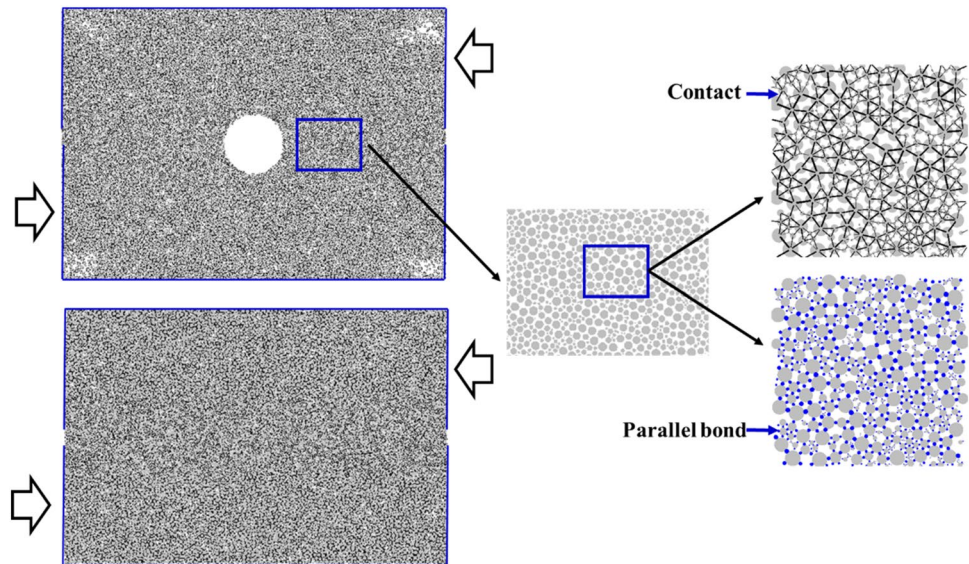


Table 5 Calibrated meso-parameters of particles in PFC^{2D} model

Meso-parameters	Values
Minimum radius of the particle, R_{min} (mm)	0.25
Ratio of maximum to minimum of radius, R_{max}/R_{min}	10
Particle density, ρ (kg/m ³)	2350
Particle friction coefficient, μ	0.97
Particle contact modulus, E_c (GPa)	0.5
Ratio of normal to shear stiffness of the particle, k_n/k_s	1.0
Parallel bond modulus, E_c' (GPa)	0.5
Ratio of normal to shear stiffness of parallel bond, K_n'/k_s'	1.0
Parallel-bond normal strengths (σ_n), mean (MPa)	40.0
Parallel-bond shear strengths (τ_n), mean (MPa)	5.0
Parallel-bond friction angle, ($^\circ$)	41.0

stress–strain curve obtained by numerical simulation. Note: In the force chain and crack evolution diagram, the magenta line represents the crack, cyan and gray areas represent tensile stress and compressive stress, respectively. In the stress distribution diagram, the maximum principal stress distribution and the minimum principal stress distribution are given by the measuring circle, and stress is expressed as tension (positive) and compressive (negative). The arrangement principles of measurement circle are related to the center position, diameter selection, arrangement density, arrangement uniformity and boundary effect. Specifically, according to the recommendation literature by Hägele et al. (2017), for a 2D model, a measurement circle should contain no less than 400 particles to ensure reliable measurement results. In

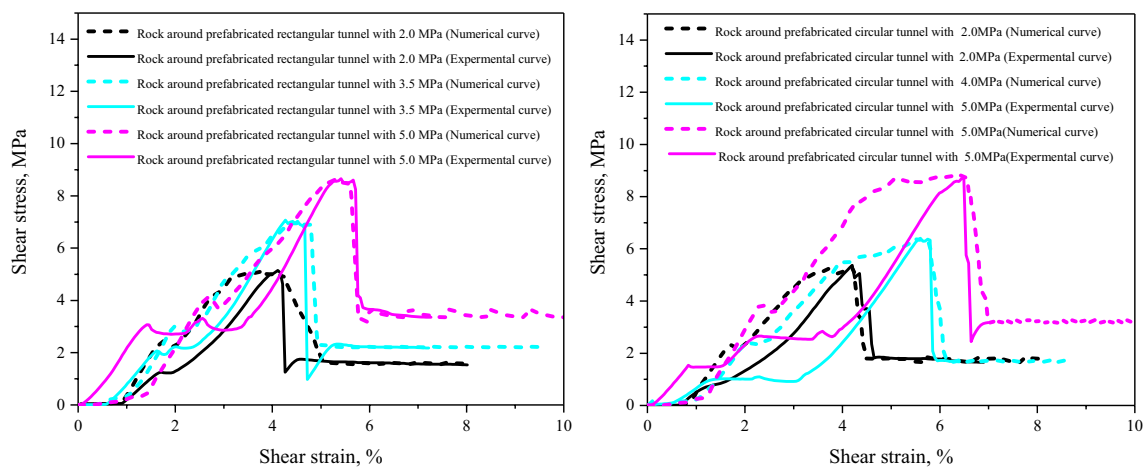


Fig. 9 Comparison of experimental and numerical results

Table 6 Failure modes of specimens

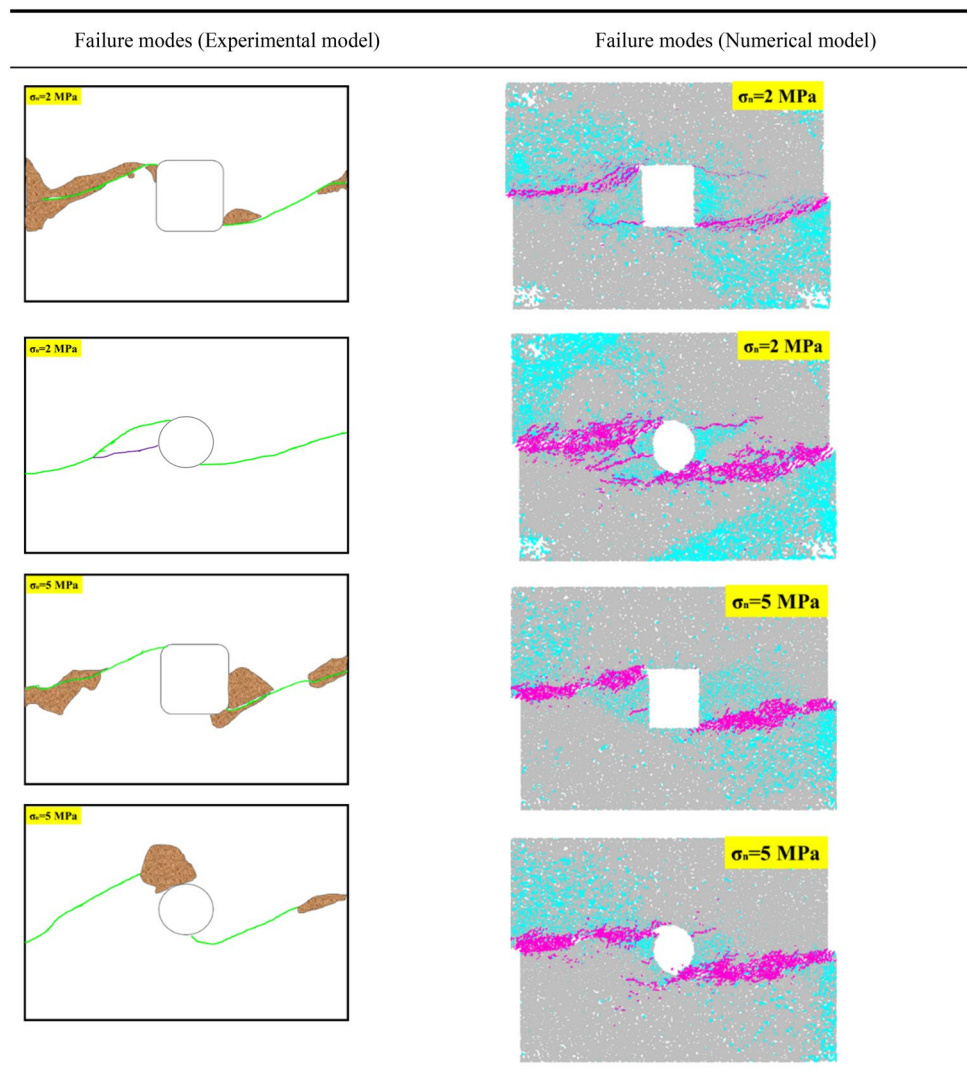


Table 7 Comparison of test results and simulation results

Sample	Experi- mental result	Numerical result	Error, %	Experimental result	Numerical result	Error, %
	τ , MPa	τ , MPa		G, MPa	G, GPa	
Rock around prefabricated rectangular tunnel with 2.0 MPa normal stress	5.24	5.26	0.39	103.52	101.32	2.12
Rock around prefabricated rectangular tunnel with 3.5 MPa normal stress	6.87	6.72	2.18	127.53	128.02	3.84
Rock around prefabricated rectangular tunnel with 5.0 MPa normal stress	8.74	8.70	4.58	101.99	101.58	4.02
Rock around prefabricated circular tunnel with 2.0 MPa normal stress	5.25	5.2	3.86	101.53	101.58	0.46
Rock around prefabricated circular tunnel with 4.0 MPa normal stress	6.51	6.46	0.77	80.58	80.21	4.59
Rock around prefabricated circular tunnel with 5.0 MPa normal stress	8.63	8.74	1.27	125.21	125.69	3.83

this study, 50 measuring circles were arranged, including an average number of 460 particles, which adheres to the principle of measuring circle arrangement. Taking the numerical models shear test with 5.0 MPa normal stress as an example, the representative failure characteristics of rock around the tunnel with section shapes were analyzed in-depth.

Shearing compaction stage (stage I): as the shear deformation increased, the shear characteristic curve presented non-linear variation. For the intact specimen with 5.0 MPa normal stress, the left upper and right lower end were in the tensile state, and the rest were in the compressive state (Table 8), due to the tensile stress concentration caused by the boundary effect (Bahaaddini 2017). For rock around tunnel with section shapes, compressive stress was widely distributed, while tensile stress was presented around the tunnel, especially in the right upper spandrel and left lower bottom of the tunnel, such as rock around prefabricated rectangular tunnel with 5.0 MPa normal stress and rock around prefabricated highway tunnel with 5.0 MPa normal stress, manifested that the arch effect caused stress concentration (Wu et al. 2022). In stage I, there was almost no micro-crack initiation, corresponded to the crack quiet period.

Linear elasticity stage (stage II): for Intact specimen with 5.0 MPa normal stress, the crack initiated first from the middle of the left side of the specimen (Table 8), where compressive stress was concentrated, but no macro-fracture surface was formed due to the limited number of micro-cracks. For rock around the tunnel with section shapes, the crack initiation was different from that of the intact specimen. The crack initiation occurred in the deviatoric stress concentration zone around the tunnel (Table 8). For example, in the rock around prefabricated rectangular tunnel with 5.0 MPa normal stress, the crack initiation occurred in the deviatoric stress concentration zone at the upper left shoulder angle, and the maximum deviatoric stress can reach about 40 MPa (Table 8). It was worth noting that the bearing capacity of the rock around prefabricated circular tunnel was lower than that of the rock around prefabricated rectangular tunnel in Sect. 3.2. Combined with the stress nephogram and displacement field of rock around prefabricated rectangular and circular tunnels, the schematic diagram of their bearing capacity was summarized (Fig. 11), and the size of the arrow manifested the strength of bearing capacity. The bearing capacity mechanism was as follows: from the upper left shoulder angle to the middle left boundary of the rock around the tunnel was a quasi-tensile-shear crack, whose crack order was relative shear crack-tensile shear crack-relative shear crack. The left upper shoulder angle and right lower shoulder angle of the rock around the tunnel were taken as examples for a detailed explanation. Specifically, relative shear crack triggered shear failure, and there was compressive stress concentration at the upper left and lower right rock around prefabricated rectangular and

circular tunnels (principal stress nephogram in Table 8). By comparing the nephogram of the maximum principal stress and the minimum principal stress, revealed that the average deviatoric stress difference was about 40 MPa, and bearing capacity was almost equal. However, the minimum principal stresses of the rock around prefabricated rectangular and circular tunnels were about 27 MPa and 33 MPa, respectively, indicating that the confining pressure of rock around prefabricated rectangular tunnel specimens was higher than that of the rock around prefabricated circular tunnel, resulting in a stronger bearing capacity than rock around prefabricated circular tunnel. Due to the stable increase of micro-cracks at stage II, some micro-cracks were coalesced to form small macro-cracks, corresponded to the crack initial increase stage.

Shearing fracture stage (stage III): for the intact specimen with 5.0 MPa normal stress, the crack coalesced from the middle of the specimen, resulting in the overall failure, belonging to the shear failure formed by the compressive stress concentration zone. For rock around tunnel with section shapes, the shear failure features were significantly different from those of intact specimen, and their failure mode was shear-dominated mixed failure. The fracture of specimen was mainly caused by the accumulation of micro-cracks subjected to shear loading. Specifically, on the left side of the specimen, the crack coalesced at the left middle end (compressive stress concentration zone) and the left upper shoulder angle of the tunnel (deviatoric stress concentration zone). On the right side of the specimen, the crack coalesced at the right middle end of the specimen (compressive stress concentration zone) and the right lower shoulder angle of the tunnel (deviatoric stress concentration zone). In addition, the number of cracks increased exponentially, and with the increment of shear deformation, the number of shear cracks was significantly larger than that of tensile cracks, which corresponded to the crack rapid increase stage.

Shearing friction stage (stage IV): different specimens revealed a similar fracturing process. After the peak shear strain, the shear stress dropped sharply, and the micro-cracks further accumulated, forming a macro-fracture zone on the shear plane. At this time, the shear fracture plane has been formed, and the friction slip occurred along the joint plane, corresponding to the crack stable stage.

To investigate the stress evolution of rock around the tunnel with section shapes subjected to shear loading, the stress state (xx direction) of key regions was monitored by measuring the circle. Figure 12 presented the change during the shearing process. Three key regions were selected, in which region A was taken as a comparison, taken from the non-stress concentration zone, and regions B and C were taken from the deviatoric stress concentration zone. In the shear process, the stress distribution of specimens with section shapes were similar, and the peak shear stress appeared at

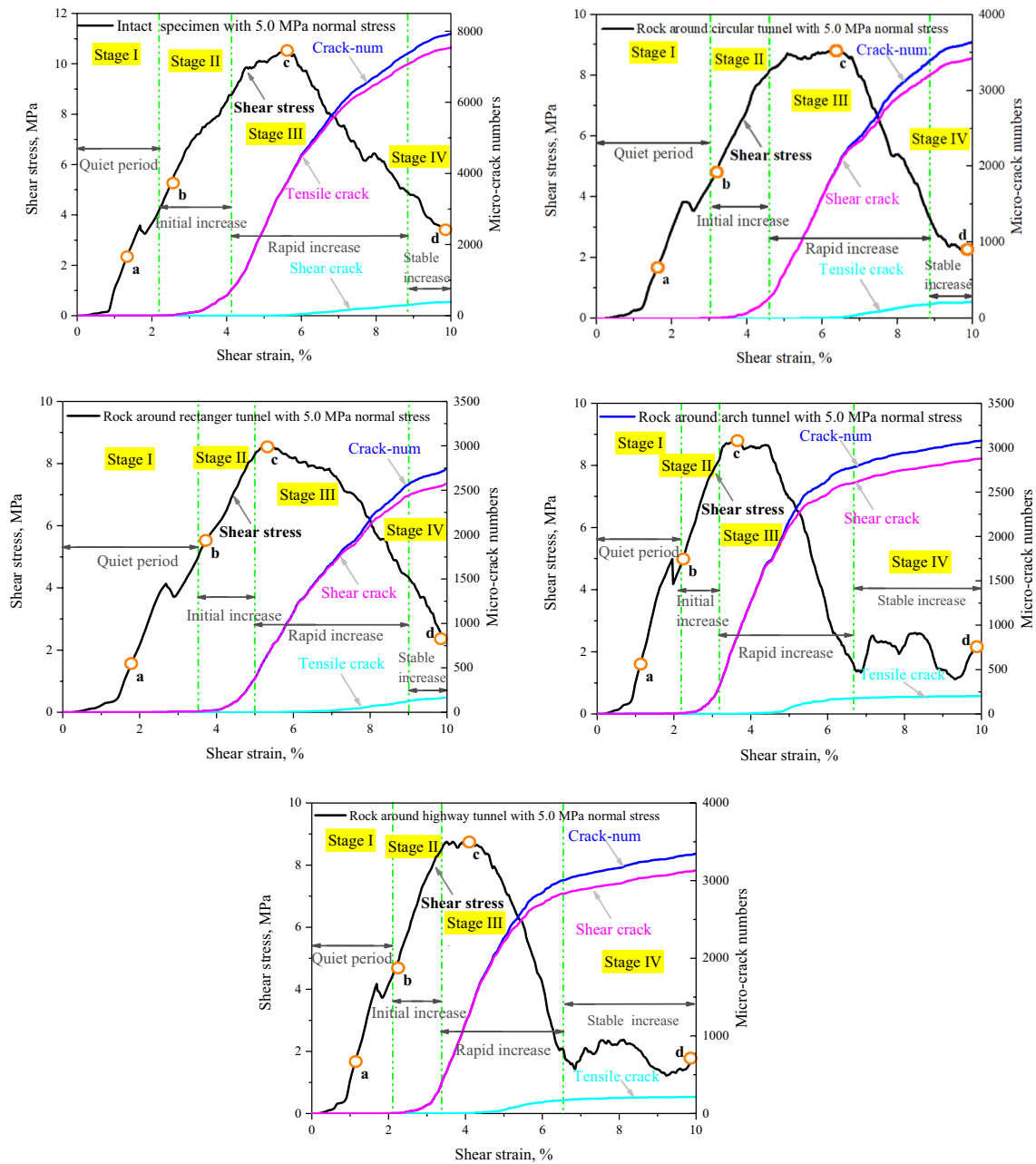


Fig. 10 Micro-cracks evolution characteristic curve

about 4% of the shear strain. After the peak strain, the stress of most specimens decreased obviously. As the loading continued, the upper and lower joint surfaces were staggered subjected to the effect of dilatancy. In addition, there was a difference in the stress between the two deviatoric compression stress concentration areas. In rock around prefabricated rectangular, circular and arch tunnels, the highest stress in region B caused the region to yield first. The stress in the region C of rock around prefabricated highway tunnel was the highest, resulting in serious damage to the right lower shoulder angle.

According to the above analysis of the crack evolution process and stress distribution, the following important characteristics can be summarized.

The shear failure mode of the rock around tunnel models (shear-dominated mixed failure) was different from that of the intact numerical model (shear failure) in Table 8, and most of the cracks were formed in stages III–IV. For rock around the tunnel with tunnel section shapes, cracks initiated around the tunnel, especially at the upper left shoulder angle. The micro-crack characteristics curve of rock around tunnel categorized into four stages, i.e. crack quiet period

Table 8 Crack evolution and stress distribution

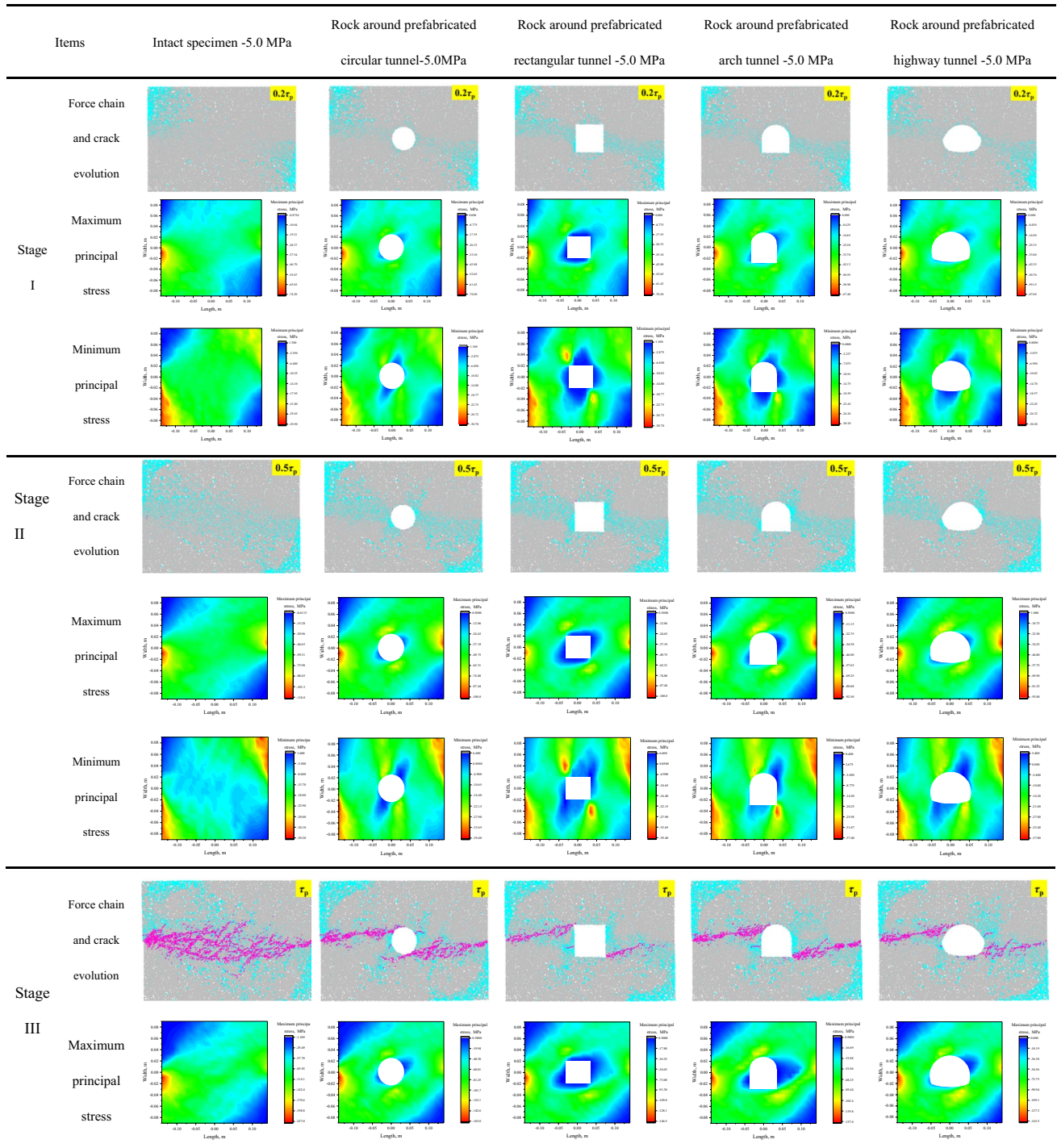
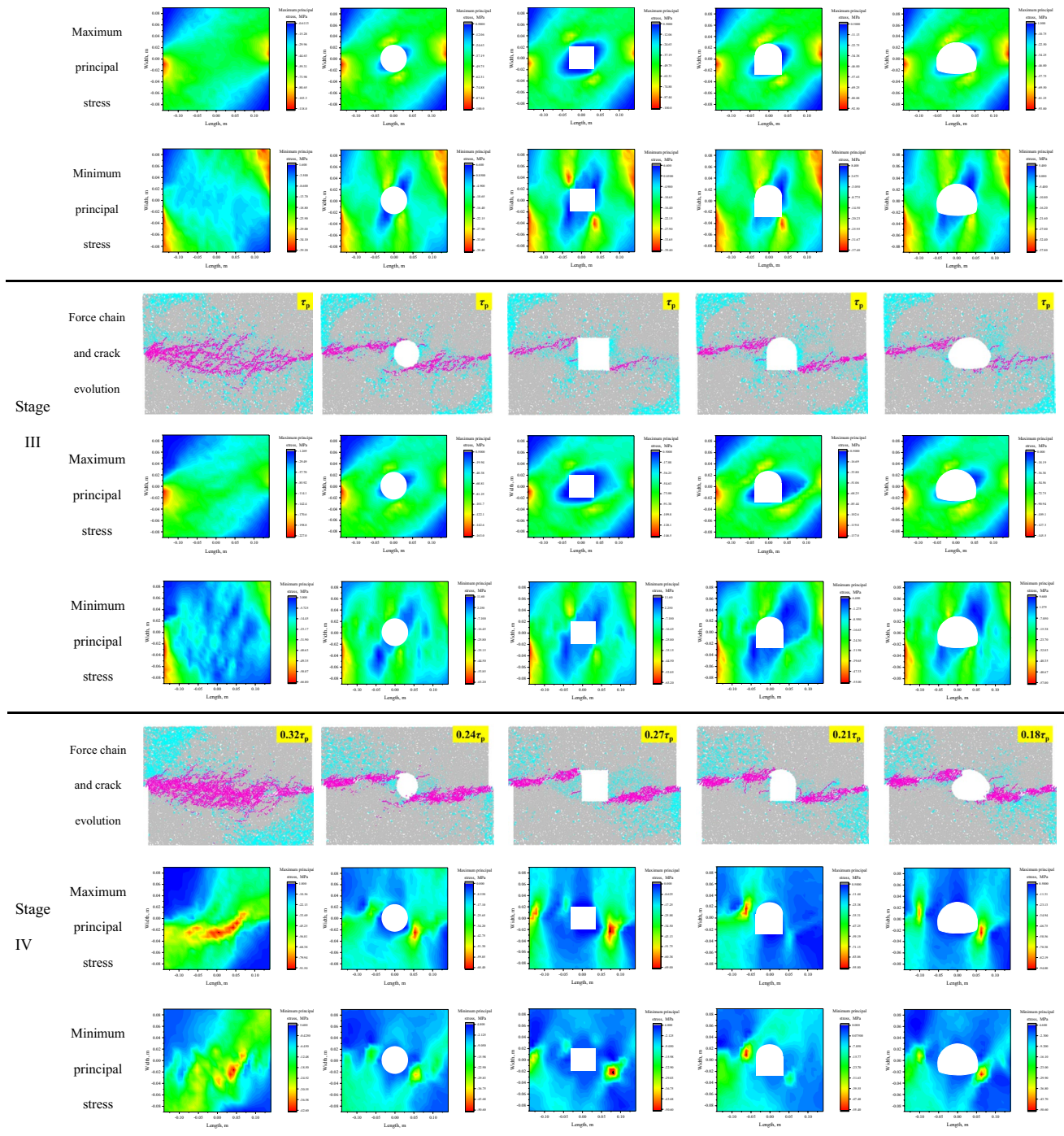


Table 8 (continued)



(stage I), crack initial increase stage (stage II), crack rapid increase stage (stage III), and crack stable stage (stage IV). In addition, shear cracks played a dominant role in the crack evolution of specimens, and the variance between the number of shear cracks and that of tensile cracks magnified with the increment of shear deformation.

4.3 Shearing Failure Mechanism

We have examined the crack evolution process and failure mode of rock around tunnel with section shapes, the fracturing mechanism was not well understood. Herein, the meso-fracture mechanism of specimens with section shapes was revealed by displacement field distribution. When the normal stress was 5.0 MPa, the displacement field of rock around the

Fig. 11 Schematic diagram of bearing capacity: **a** rock around prefabricated circular tunnel, **b** rock around prefabricated rectangular tunnel

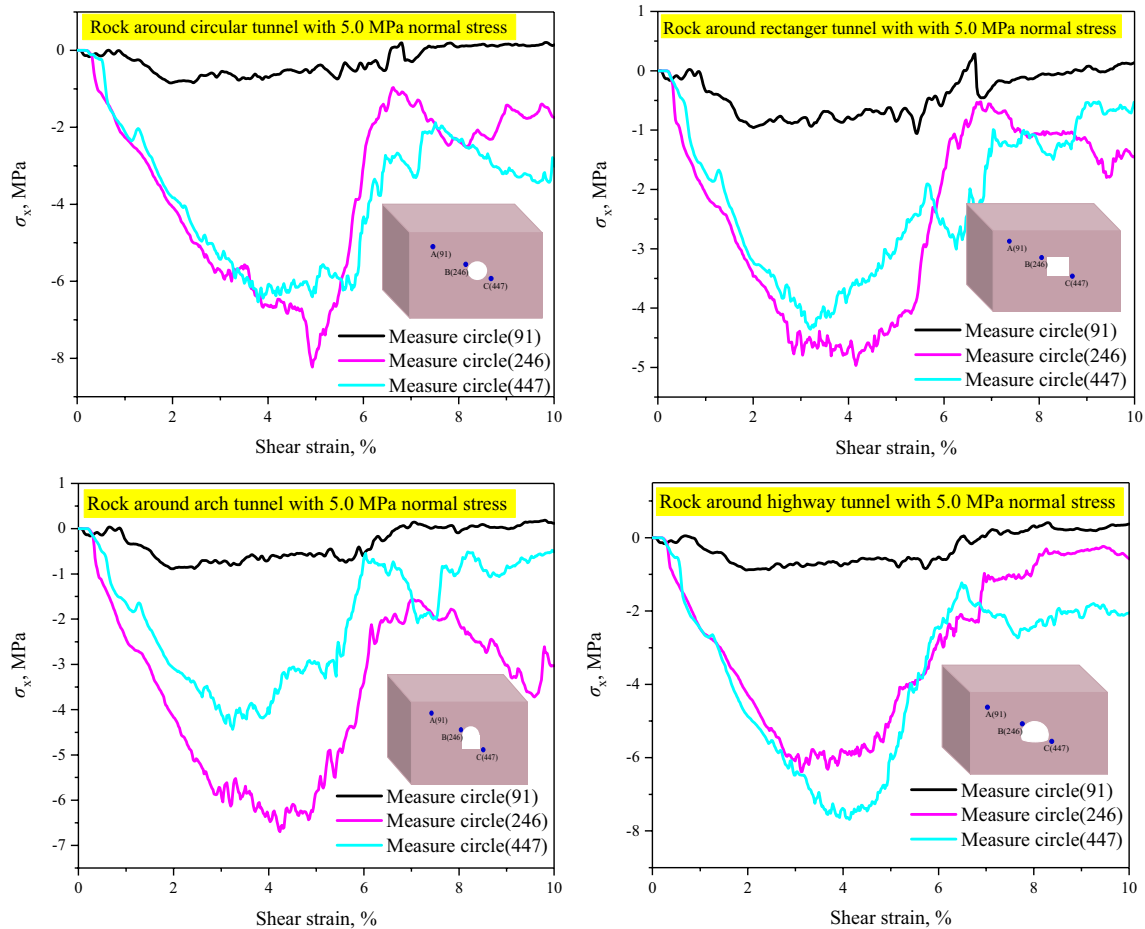
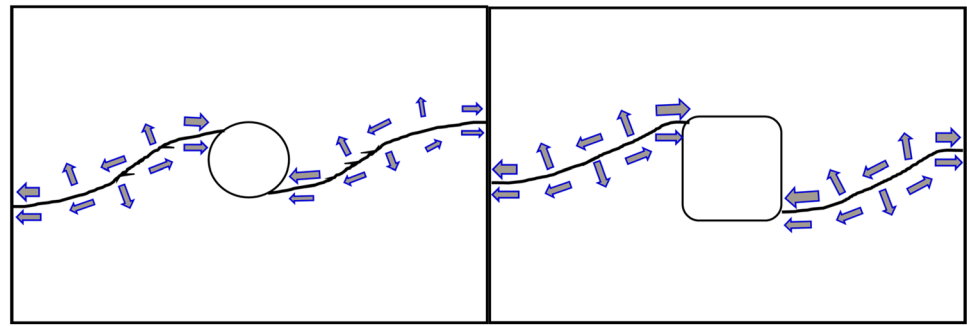


Fig. 12 Stress evolution (xx direction) of rock around tunnel with section shapes

tunnel with section shapes subjected to shear loading were shown in Fig. 13. Both rock around prefabricated rectangular and circular tunnels carved obvious displacement interfaces, which was consistent with the laboratory macro-shear fracture, proving the availability of numerical simulation. To better comprehend the origin of different macro-crack types, enlarged images of different typical macro-cracks were given, which depicted the displacement size and direction of particles on both sides of the macro-cracks.

In terms of the displacement direction and size of particles on both sides of the crack, the crack type was determined (Zhang and Wong 2014). Six main micro-cracking mechanism types were summarized: direct tensile crack (DT), relative tensile crack (RT), direct tensile crack (DS), relative shear crack (RS), tensile shear crack (ST), and block rotation (BR). It can be found that the cracks were tensile-shear mixed cracks from the left middle of the rock around tunnel with section shapes to the upper left shoulder angle of

the tunnel, characterized by relative tensile crack, as shown in Fig. 13a, d and e. Specifically, the tensile crack portion was mainly dominated by direct tensile crack and relative tensile crack, while the shear crack was controlled by direct tensile crack. The block rotation appeared in the right middle of rock around tunnel with section shapes, characterized by BR, as shown in Fig. 13b, c. In general, direct tensile crack, relative tensile crack or tensile shear crack would lead to tensile cracks, while direct tensile crack and relative shear crack will trigger shear cracks. The macro-shear failure of rock around tunnel with section shapes was mainly shear-dominated mixed failure. The numerical results clearly revealed that DEM well reproduced the shear behavior of rock with tunnel, and presented the ability to investigate the

shear mechanism. It also provided a useful tool for predicting the shear behavior of rock mass.

5 Discussion

5.1 Energy Analysis

5.1.1 Damage Characteristic

When the rock is intact state, the dissipation strain energy is zero, leading to the damage variable value is 0; when the rock is fully damaged, the dissipation strain energy tends to infinity, causing damage variable value is 1 (Zhao et al. 2020). The following is based on the fact that the damage

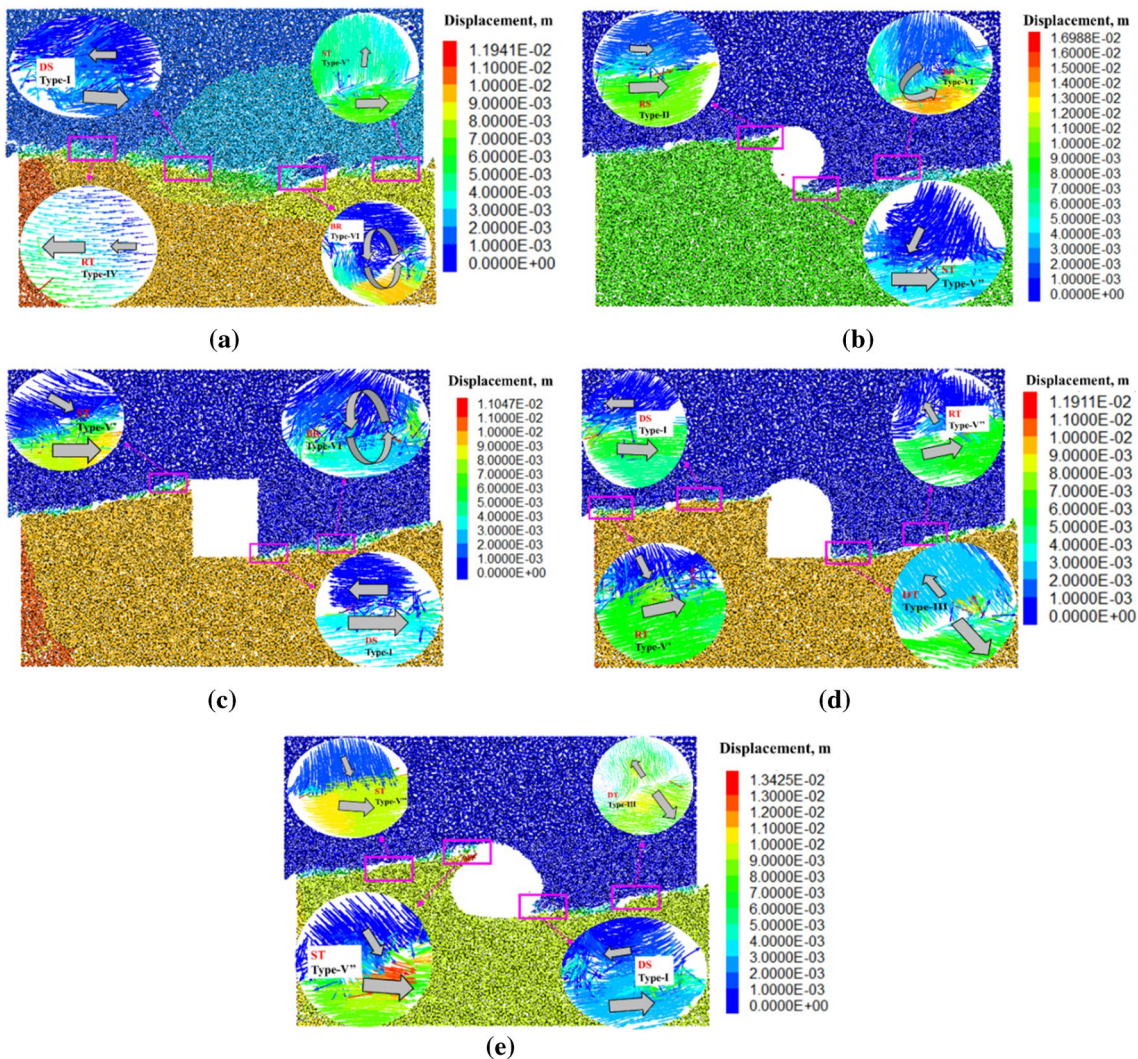


Fig. 13 Displacement field distribution of rock around tunnel with section shapes: **a** intact specimen with 5.0 MPa normal stress, **b** rock around prefabricated circular tunnel with 5.0 MPa normal stress, **c** rock around prefabricated rectangular tunnel with 5.0 MPa normal

stress, **d** rock around prefabricated arch tunnel with 5.0 MPa normal stress, **e** rock around prefabricated highway tunnel with 5.0 MPa normal stress

variable is from 0 to 1, so the inverse trigonometric function is selected. More importantly, the ratio of dissipative strain energy increment to shear stress increment is the nominal plastic strain. Therefore, on the basis of the evolution relationship between shear stress and dissipation strain energy, a novel damage variable is defined as follows:

$$D = \frac{2}{\pi} \operatorname{arccot} \left(-\frac{\Delta U_d}{\Delta \tau} \right) - 1, \quad (4)$$

where $\Delta \tau$ is shear stress increment, ΔU_d is the corresponding dissipative strain energy increment.

Figure 14 displays the damage evolution of rock around prefabricated rectangular and circular tunnels with normal stresses. The overall trend of the damage evolution can be summarized as follows: the slope of the damage evolution curve at the beginning was gentle, but with the increment of shear strain, the damage level of the specimens gradually intensified. When the shear strain reached the peak strain, the curve suddenly bended upward, indicating that the damage variable increased rapidly. This caused the bearing capacity of the specimen lost sharply until it was completely damaged. Under the same normal stress, the damage variable of rock around prefabricated circular tunnel specimens was greater than that of rock around prefabricated rectangular tunnel. This indicated that the damage level of rock around prefabricated circular tunnel specimens was more serious than that of rock around prefabricated rectangular tunnel, aligned with the fracture behavior of rock around the tunnel in Sect. 3.3

5.1.2 Energy Criterion

Rockburst is a violent disaster accompanied by the ejection of broken rock fragments (Kaiser and Cai 2012; Zhou et al. 2018). To evaluate the rockburst tendency, it was necessary to analyze the rockburst phenomenon of rock through laboratory tests. During the shear test, a high-speed camera was adopted to capture the ejection process of rock fragments, such as internal fracture characteristics in Sect. 3.3. On the one hand, the ejection velocity of rock fragments can be evaluated according to the ejection time and distance recorded by a high-speed camera. On the other hand, with reference to the failure phenomenon of the specimens recorded, the number of ejection fragments, the sound of ejection and the failure mode can be counted.

The failure mode, ejection velocity, ejection sound and ejected fragments quantity of rock around the tunnel were collected and listed in Table 9. Under normal stresses, the rock around the tunnel exhibited shear-induced rockburst. Compared with the specimens with low normal stress

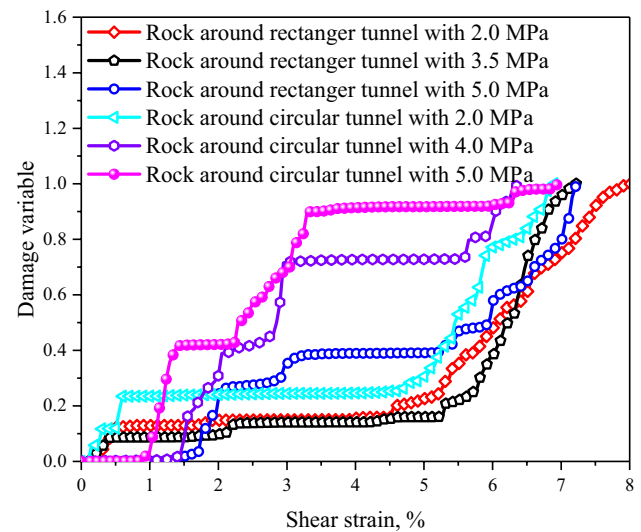


Fig. 14 Damage evolution curves of rock around tunnel with different tunnel section shapes

(2.0 MPa), the ejection velocity and the sound level of the specimens with high normal stress was lower, and a small amount of rock fragments was observed, indicating that the rockburst tendency of rock around the tunnel with high normal stress (5.0 MPa) was lower. For rock around the tunnel with low normal stress, a large number of rock fragments were ejected in a piercing sound subjected to shear loading, and the velocity of ejection was above 4.24–4.86 m/s. These phenomena manifested that the rockburst tendency was high.

In the light of the idea of the impact tendency index of rock loading and unloading process (Kidybiński 1981), a novel impact tendency index ($S_{p\ et}$) subjected to shear condition was proposed to evaluate shear-induced rockburst, as shown in Eq. (5), and the specific diagram was depicted in Fig. 15. The criteria for shear-induced rockburst is different from that of stress-induced rockburst, so the classification criteria value of rockburst tendency should be reclassified into four grades: high rockburst, middle rockburst, low rockburst, and no rockburst, as shown in Eq. (6). The division was based on the division of the impact tendency index of stress-induced rockburst (Chai et al 2023) and the dynamic phenomenon of shear-induced rockburst in laboratory tests, and the specific results were shown in Table 9.

$$S_{p\ et}^D = U_e^p / U_d^p, \quad (5)$$

where $S_{p\ et}$ is the impact tendency index subjected to shear condition, U_e^p and U_d^p are the elastic strain energy and dissipated strain energy at the shear peak stress.

Table 9 Ejection characteristics of rock around tunnel specimens

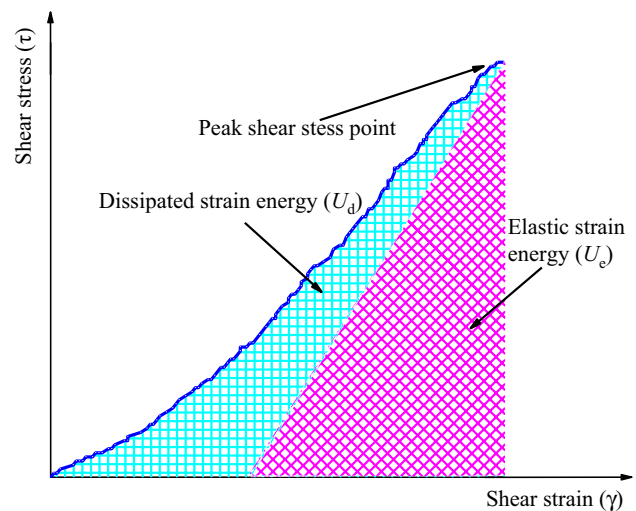
Items	Failure mode	Ejection speed, m/s	Ejection sound	Ejected fragments quantity	Sp et	Rock-burst tendency
Rock around prefabricated rectangular tunnel with 2.0 MPa normal stress	Shear-dominated mixed failure	4.86	Loud	Great	5.23	High
Rock around prefabricated rectangular tunnel with 3.5 MPa normal stress		3.11	Middle	Major	3.47	Middle
Rock around prefabricated rectangular tunnel with 5.0 MPa normal stress		2.51	Slight	Minor	2.20	Low
Rock around prefabricated circular tunnel with 2.0 MPa normal stress		4.24	Loud	Great	4.83	High
Rock around prefabricated circular tunnel with 4.0 MPa normal stress		3.19	Middle	Major	3.48	Middle
Rock around prefabricated circular tunnel with 5.0 MPa normal stress		1.96	Slight	Minor	1.92	Low

$$\left. \begin{array}{l}
 S_{et}^p > 5 \text{ High rock burst proneness} \\
 3.5 < S_{et}^p \leq 5 \text{ Middlerock burst proneness} \\
 2 < S_{et}^p \leq 3.5 \text{ Low rock burst proneness} \\
 S_{et}^p < 2 \text{ No rock burst proneness}
 \end{array} \right\} \quad (6)$$

With reference with the elastic strain energy and dissipative strain energy at the peak stress, the impact tendency index (S_{pe}) of the rock around prefabricated rectangular tunnel specimens was always higher than that of the rock around prefabricated circular tunnel. For example, the results of the impact tendency index (S_{pe}) of rock around prefabricated rectangular tunnel specimen with 2.0 MPa normal stress and rock around prefabricated circular tunnel with 2.0 MPa normal stress were 5.23 and 5.03 respectively, also proved by the phenomenon observed by high-speed cameras. Compared with the rock around prefabricated circular tunnel specimens, the rock around prefabricated rectangular tunnel specimens exhibited higher ejection speed, higher sound level and a large number of rock fragments observed, indicating that the rock around prefabricated rectangular tunnel specimens was more severely damaged. This was consistent with the analysis in Sect. 3.3. Moreover, the above analysis revealed that reasonable tunnel section reduced the rockburst tendency. Meanwhile, the shear-induced rockburst tendency of other specimens was also listed in Table 9.

5.2 Shearing Conceptual Model

Shear interface properties of rock around the tunnel are affected not only by the cohesion and internal friction Angle but also by meso-structure of the interface such as grooves and protrusions. On the ground of meso-morphology of

**Fig. 15** Calculation of energy at peak shear stress

the interface, it was generalized as the undulating interface with groove structure, which originated ‘self-locking’ effect (Zhang et al. 2020), such as stepped interface, zigzag interface and V-shaped interface.

Subjected to compression-shear condition, carbonate cementitious materials bond quartz, feldspar, debris and other materials to form a V-shaped skeleton, which was closely filled with debris on the undulating interface, as shown in Fig. 16. When the interface groove was filled with scattered minerals such as quartz, the minerals in the groove were locked to form ‘lock structure’ (Wenjie and Shi 2016). The two-peak vertex connection of the groove structure was the locking structure interface line. The mineral aggregate was mainly subjected to the overlying pressure under the lock structure interface line. When there was no hard mineral such as quartz scattered on the lock structure interface line, the groove was filled with debris and acted as

the bedrock interface. The plane shear occurred herein, i.e., the lock structure ‘failed’, as shown in Fig. 16a. When there were hard minerals such as quartz scattered on the interface line, due to the locking effect, the mineral aggregates at the lower part of the interface line were locked in the groove, and the hard minerals of the interface were sheared. If the shear strength of the hard mineral was lower than the shear stress, the shear failure occurred at the stress interface. If it was higher than the shear stress, it was embedded with the bedrock interface. And the hard mineral on the interface line acted as an interface convex structure. The bedrock near such hard minerals was sheared by shear stress, as shown in Fig. 16b, c.

The external contour of ‘locking structure’ tended to arch, which was due to the fact that the shear band formed by the turnover displacement of debris particles on the external contour of the ‘locking structure’, and the debris particles were extremely difficult to overturn in a vertical height beyond their radius. Therefore, the convex structure caused by scattered hard minerals would be continuously filled and recombined by bedrock to form a smooth arched shear channel, which was convenient for subsequent debris to rotate over the convex structure.

6 Conclusions

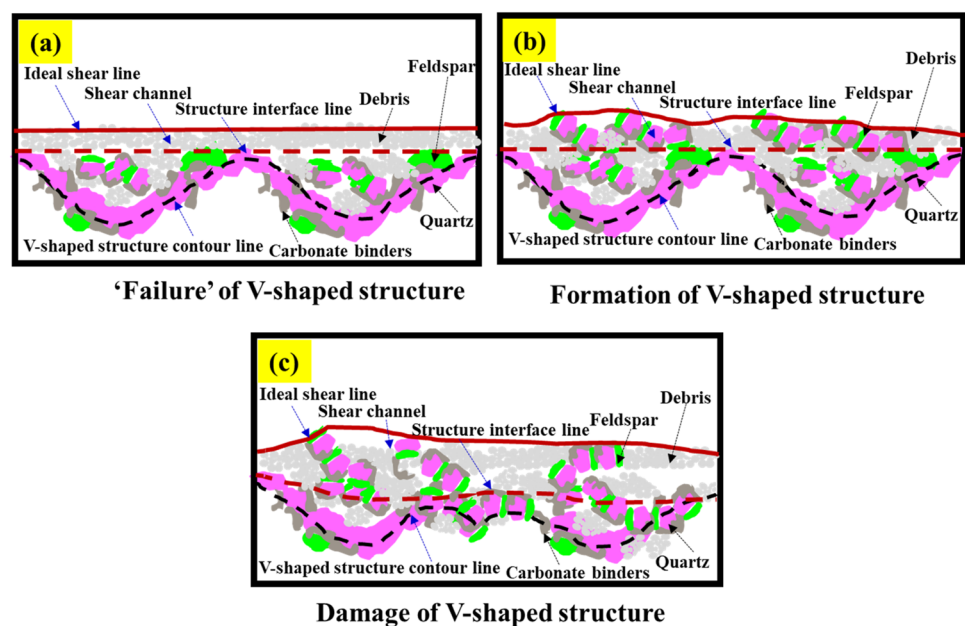
A series of physical model shear tests were conducted to exploit the shear fracturing process of rock around prefabricated rectangular and circular tunnels. And, mechanical behavior and fracturing of rock around tunnel were systematically recorded by a high-speed camera and acoustic

emission monitor. In light of DEM, the established numerical model successfully reproduced the mechanical behavior and analyzed the fracturing mechanism. On the ground of the first law of thermodynamics, the energy conversion process, damage characteristics and rockburst tendency of rock around tunnel were investigated, and the following conclusions were summarized.

In the shear test, the shear characteristic of rock around tunnel specimens generally was classified as four stages. The specimens went through the shearing compression stage (stage I), elastic stage (stage II) dominated by crack initiation, shearing fracture stage (stage III) dominated by crack propagation, coalescence and shear-induced rockburst, and the shearing friction stage (stage IV). The difference was that rock around prefabricated circular tunnel concentrated on the vault and arch bottom, while the rock around prefabricated rectangular tunnel paid attention to the upper right shoulder angle and the lower left shoulder angle. It was emphasized that the damage stress and rockburst tendency of rock around prefabricated rectangular tunnels were superior to those of rock around prefabricated circular tunnels, related to the similar deviatoric stress distribution, but confining pressure of rock around prefabricated rectangular tunnel was higher than that of rock around prefabricated circular tunnel.

In the shear test, the energy characteristic conversion of rock around tunnel was divided into four stages, corresponding to the shear characteristic. The energy characteristic conversion manifested that the rock around tunnel specimens were mainly elastic deformation before peak shearing load, and the plastic deformation was relatively small. Partial dissipated strain energy acted on closing hole and crack initiation, and the rest was stored as elastic strain energy. After the peak shearing

Fig. 16 Shearing mechanism conceptual model



load, the shear strength of the specimens dropped rapidly, and a large amount of strain energy was converted into dissipated strain energy for crack propagation, coalescence, and shear-induced rockburst. The larger the elastic strain energy release rate was, the more fragments triggered by rock breaking, and the higher rockburst tendency. In addition, a novel damage variable was proposed to quantify the damage degree of rock. And, a novel impact tendency index (Sp_{et}) was presented for evaluating the shear-induced rockburst tendency, revealed the proportional relationship between elastic strain energy and dissipative strain energy at peak shearing load.

In the numerical shear test, the four stages of rock around the tunnel were successfully reproduced, and the shear fracturing process of rock around tunnel specimens with tunnel section shapes were analyzed in-depth. It was found that the failure mode of rock around tunnel specimens (shear-dominated mixed failure) was different from that of the intact model (shear failure), and most of the cracks were initiated in stages III–IV. For the specimens with different tunnel section shapes, cracks initiated around the tunnel, especially at the upper left shoulder angle. In addition, in line with the four stages of shear characteristic, the micro-crack evolution of the rock around tunnel model was classified into four stages, i.e. crack quiet period (stage I), crack initial increase stage (stage II), crack rapid increase stage (stage III), and crack stable stage (stage IV). And, shear cracks played a dominant role in the crack evolution of the specimens, and the variance between the number of shear cracks and that of tensile cracks magnified with the increment of shear deformation.

Acknowledgements The authors gratefully acknowledge the financial support from the National Natural Science Foundation of China (No. 52325905) and the Open Research Fund of State Key Laboratory of Geomechanics and Geotechnical Engineering, Institute of Rock and Soil Mechanics, Chinese Academy of Sciences (No. Z020005).

Author Contributions JX conceptualization, methodology, writing-original draft, and writing-review and editing; QJ conceptualization, resources, supervision, and funding acquisition; SL resources, supervision, and data curation; PC resources, formal analysis; HZ resources, formal analysis.

Data availability Data will be made online as requested.

Declarations

Conflict of interest The authors declare that there is no conflict of interest concerning the publication of this paper.

References

AC10520942 (2008) Standard test method for performing laboratory direct shear strength tests of rock specimens under constant normal force. ASTM

- Aydin A (2009) The ISRM suggested methods for rock characterization, testing and monitoring: 2007–2014. *Int J Rock Mech Min Sci* 46:627–634
- Bahaaddini M (2017) Effect of boundary condition on the shear behaviour of rock joints in the direct shear test. *Rock Mech Rock Eng* 50:1141–1155
- Bieniawski Z (1967) Mechanism of brittle fracture of rock: part I—theory of the fracture process. *Int J Rock Mech Min Sci Geomech Abstr* 4:395–406
- Brady B, Rowell G (1986) Laboratory investigation of the electro-dynamics of rock fracture. *Nature* 321:488–492
- Bratov V, Petrov Y (2007) Optimizing energy input for fracture by analysis of the energy required to initiate dynamic mode I crack growth. *Int J Solids Struct* 44:2371–2380
- Cao R, Cao P, Fan X, Xiong X, Lin H (2016a) An experimental and numerical study on mechanical behavior of ubiquitous-joint brittle rock-like specimens under uniaxial compression. *Rock Mech Rock Eng* 49:4319–4338
- Cao R, Cao P, Lin H, Pu C, Ou K (2016b) Mechanical behavior of brittle rock-like specimens with pre-existing fissures under uniaxial loading: experimental studies and particle mechanics approach. *Rock Mech Rock Eng* 49:763–783
- Chai Y, Dou L, Cai W, Małkowski P, Li X, Gong S, Bai J, Cao J (2023) Experimental investigation into damage and failure process of coal-rock composite structures with different roof lithologies under mining-induced stress loading. *Int J Rock Mech Min Sci* 170:105479
- Chen S, Xia Z, Feng F, Yin D (2021) Numerical study on strength and failure characteristics of rock samples with different hole defects. *Bull Eng Geol Environ* 80:1523–1540
- Colombo D, Massin P (2011) Fast and robust level set update for 3D non-planar X-FEM crack propagation modelling. *Comput Method Appl Mech* 200:2160–2180
- Cornetti P, Pugno N, Carpinteri A, Taylor D (2006) Finite fracture mechanics: a coupled stress and energy failure criterion. *Eng Fract Mech* 73:2021–2033
- Debecker B, Vervoort A (2013) Two-dimensional discrete element simulations of the fracture behaviour of slate. *Int J Rock Mech Min Sci* 61:161–170
- Fan X, Li K, Lai H, Xie Y, Cao R, Zheng J (2018) Internal stress distribution and cracking around flaws and openings of rock block under uniaxial compression: a particle mechanics approach. *Comput Geotech* 102:28–38
- Fan X, Yu H, Deng Z, He Z, Zhao Y (2022) Cracking and deformation of cuboidal sandstone with a single nonpenetrating flaw under uniaxial compression. *Theor Appl Fract Mech* 119:103284
- Fedotova IV, Kuznetcov N, Pak A (2017) Specific strain energy assessment of hard rocks under different loading modes. *Proc Eng* 191:317–323
- Feng X, Kong R, Zhang X, Yang C (2019) Experimental study of failure differences in hard rock under true triaxial compression. *Rock Mech Rock Eng* 52:2109–2122
- Ferro G (2006) On dissipated energy density in compression for concrete. *Eng Fract Mech* 73:1510–1530
- Griffith A (1921) The phenomena of rupture and flow in solids. *Philos Trans R Soc Lond Ser A* 221:163–198
- Hägele A, Hall S, Sullivan C (2017) Efficient measurement strategies for particle flow simulations: the influence of circle arrangement on accuracy and efficiency. *Geotechnique* 67(11):986–997
- Haijian S, Hongwen J, Honghui Z, Yingchao W (2014) Experimental study on the influence of longitudinal fissure on mechanics characteristic of sandstone. *J Min Saf Eng* 31:644
- Han Z, Li D, Zhou T, Zhu Q, Ranjith P (2020) Experimental study of stress wave propagation and energy characteristics across rock specimens containing cemented mortar joint with various thicknesses. *Int J Rock Mech Min Sci* 131:104352

- Horii H, Nemat S (1985) Compression-induced microcrack growth in brittle solids: axial splitting and shear failure. *J Geophys Res Sol EA* 90:3105–3125
- Huang D, Li Y (2014) Conversion of strain energy in triaxial unloading tests on marble. *Int J Rock Mech Min Sci* 66:160–168
- Huang Y, Yang S, Ranjith P, Zhao J (2017) Strength failure behavior and crack evolution mechanism of granite containing pre-existing non-coplanar holes: experimental study and particle flow modeling. *Comput Geotech* 88:182–198
- Huang S, Liu Y, Guo Y, Zhang Z, Cai Y (2019) Strength and failure characteristics of rock-like material containing single crack under freeze-thaw and uniaxial compression. *Cold Reg Sci Technol* 162:1–10
- Jaeger C (1979) *Rock mechanics and engineering*. Cambridge University Press, Cambridge
- Jiang Q, Feng X, Fan Y, Fan Q, Liu G, Pei S, Duan S (2017) In situ experimental investigation of basalt spalling in a large underground powerhouse cavern. *Tunn Undergr Space Technol* 68:82–94
- Jiang Z, Dou C, Zhang A, Wang Q, Wu Y (2019) Experimental study on earthquake-resilient prefabricated cross joints with L-shaped plates. *Eng Struct* 184:74–84
- Jiang Q, Xin J, Xu D, Liu Q (2022) Shear failure process of rectangular tunnel: physical experimental test and numerical back-analysis. *Theor Appl Fract Mech* 120:103384
- Kaiser PK, Cai M (2012) Design of rock support system under rockburst condition. *J Rock Mech Geotech* 4:215–227
- Kidybiński A (1981) Bursting liability indices of coal. *Int J Rock Mech Min Sci Geomech Abstr* 4:295–304
- Li S, Feng X, Li Z, Chen B, Zhang C, Zhou H (2012) In situ monitoring of rockburst nucleation and evolution in the deeply buried tunnels of Jinping II hydropower station. *Eng Geol* 137:85–96
- Li X, Li C, Cao W, Tao M (2018) Dynamic stress concentration and energy evolution of deep-buried tunnels under blasting loads. *Int J Rock Mech Min Sci* 104:131–146
- Liu C, Jiang Q, Xin J, Wu S, Liu J, Gong F (2022a) Shearing damage evolution of natural rock joints with different wall strengths. *Rock Mech Rock Eng* 55:1599–1617
- Liu Q et al (2022b) Mechanical characteristics of single cracked limestone in compression-shear fracture under hydro-mechanical coupling. *Theor Appl Fract Mech* 119:103371
- Liu X, Zhang K, Liu W, Xie J (2022c) Influence of weak inclusions on the cracking behavior of a jointed rock mass containing an opening: insights from DIC-based approaches. *Arch Civ Mech Eng* 22:1–25
- Nakatani M (2001) Conceptual and physical clarification of rate and state friction: Constitutive equations and steady-state properties. *J Geophys Res Solid Earth* 106(B5):8485–8502
- Ortlepp W, Stacey T (1994) Rockburst mechanisms in tunnels and shafts. *Tunn Undergr Space Technol* 9:59–65
- Pan P, Feng X, Hudson JA (2009) Study of failure and scale effects in rocks under uniaxial compression using 3D cellular automata. *Int J Rock Mech Min Sci* 46:674–685
- Potyondy D, Cundall P (2004) A bonded-particle model for rock. *Int J Rock Mech Min Sci* 41:1329–1364
- Rahimi R, Nygaard R (2015) Comparison of rock failure criteria in predicting borehole shear failure. *Int J Rock Mech Min Sci* 79:29–40
- Ruan S, Liu L, Zhu M et al (2023) Development and field application of a modified magnesium slag-based mine filling cementitious material. *J Clean Prod* 419:138269
- Sun B (2021) a combined discrete element-finite difference model for simulation of double shield TBM excavation in jointed rocks. *Rock Mech Rock Eng* 54:5867–5883
- Wang Y, Cui F (2018) Energy evolution mechanism in process of Sandstone failure and energy strength criterion. *J Appl Geophys* 154:21–28
- Wang J, Yan H (2012) DEM analysis of energy dissipation in crushable soils. *Soils Found* 52:644–657
- Wang C, Tannant D, Lilly P (2003) Numerical analysis of the stability of heavily jointed rock slopes using PFC^{2D}. *Int J Rock Mech Min Sci* 40:415–424
- Wang S, Tang Y, Wang S (2021) Influence of brittleness and confining stress on rock cuttability based on rock indentation tests. *J Cent South Univ* 28:2786–2800
- Wang T, Yan C (2023) Investigating the influence of water on swelling deformation and mechanical behavior of mudstone considering water softening effect. *Eng Geol* 318:107102
- Wang T, Gao R, Yan C (2023a) Dynamic fragmentation and chip formation of water-soaked rock in linear cutting with a coupled moisture migration-fracture model. *Comput Geotech* 163:105723
- Wang T, Yan C, Zheng H et al (2023b) Optimum spacing and rock breaking efficiency of TBM double disc cutters penetrating in water-soaked mudstone with FDEM. *Tunn Undergr Sp Technol* 138:105174
- Wenjie X, Shi W (2016) Meso-mechanics of soil-rock mixture with real shape of rock blocks based on 3D numerical direct shear test. *Chin J Rock Mech Eng* 35:2152–2160
- Whitworth A, Vaughan J, Southam G, van der Ent A, Nkrumah P, Ma X, Parbhakar A (2022) Review on metal extraction technologies suitable for critical metal recovery from mining and processing wastes. *Miner Eng* 182:107537
- Wong R, Lin P (2015) Numerical study of stress distribution and crack coalescence mechanisms of a solid containing multiple holes. *Int J Rock Mech Min Sci* 79:41–54
- Wu Z, Wong LNY (2013) Modeling cracking behavior of rock mass containing inclusions using the enriched numerical manifold method. *Eng Geol* 162:1–13
- Wu H, Kulatilake P, Zhao G, Liang W (2019) Stress distribution and fracture evolution around a trapezoidal cavity in sandstone loaded in compression. *Theor Appl Fract Mech* 104:102348
- Wu H, Dai B, Cheng L, Lu R, Zhao G, Liang W (2021) Experimental study of dynamic mechanical response and energy dissipation of rock having a circular opening under impact loading. *Min Metall Explor* 38:1111–1124
- Wu J, Liao S, Liu M, He J (2022) Analytical investigation on the arching effect of tunnel face in sandy ground. *Tunn Undergr Space Technol* 119:104207
- Xie H, Wang J, Kwaśniewski M (1999) Multifractal characterization of rock fracture surfaces. *Int J Rock Mech Min Sci* 36:19–27
- Xiong X, Li B, Jiang Y, Koyama T, Zhang C (2011) Experimental and numerical study of the geometrical and hydraulic characteristics of a single rock fracture during shear. *Int J Rock Mech Min Sci* 48:1292–1302
- Xin J, Jiang Q, Gong F, Liu L, Liu C, Liu Q, Yang Y, Chen P (2024) Mechanical behaviors of backfill-rock composites: physical shear test and back-analysis. *J Rock Mech Geotech Eng* 16(4)
- Xu G, He C, Wang J, Zhang J (2020a) Study on the damage evolution of secondary tunnel lining in layered rock stratum. *Bull Eng Geol Environ* 79:3533–3557
- Xu H, Qin Y, Wang G, Fan C, Wu M, Wang R (2020b) Discrete element study on mesomechanical behavior of crack propagation in coal samples with two prefabricated fissures under biaxial compression. *Powder Technol* 375:42–59
- Yang S, Tian W, Huang Y, Ranjith P, Ju Y (2016) An experimental and numerical study on cracking behavior of brittle sandstone containing two non-coplanar fissures under uniaxial compression. *Rock Mech Rock Eng* 49:1497–1515

- Yang Z, Jiang Y, Li S, Li J, Hu Y (2020) Experimental study on shear mechanical properties of soil-rock mixture-bedrock interface. *Chin J Geotech Eng* 42:1947–1954
- Yang B, Jiang Q, Feng X, Xin J, Xu D (2022) Shear testing on rock tunnel models under constant normal stress conditions. *J Rock Mech Geotech* 14(6):1722–1736
- Yang P, Liu L, Suo Y, Qu H, Xie G, Zhang X, Deng S, Lv Y (2023) Investigating the synergistic effects of magnesia-coal slag based solid waste cementitious materials and its basic characteristics as a backfill material. *Sci Total Environ* 880:163209
- Yue Z, Peng L, Yue X, Wang J, Lu C (2020) Experimental study on the dynamic coalescence of two-crack granite specimens under high loading rate. *Eng Fract Mech* 237:107254
- Zhang X, Wong L (2014) Displacement field analysis for cracking processes in bonded-particle model. *Bull Eng Geol Environ* 73:13–21
- Zhang Y, Chen B, Liu A, Pi Y, Zhang J, Wang Y, Zhong L (2019a) Experimental study on shear behavior of high strength bolt connection in prefabricated steel-concrete composite beam. *Compos Part B Eng* 159:481–489
- Zhang Y, Feng X, Yang C, Zhang X, Sharifzadeh M, Wang Z (2019b) Fracturing evolution analysis of Beishan granite under true triaxial compression based on acoustic emission and strain energy. *Int J Rock Mech Min Sci* 117:150–161
- Zhang Y, Feng X, Zhang X, Wang Z, Sharifzadeh M, Yang C, Kong R, Zhao J (2019c) Strain energy evolution characteristics and mechanisms of hard rocks under true triaxial compression. *Eng Geol* 260:105222
- Zhang Y, Jiang Y, Asahina D, Wang C (2020) Experimental and numerical investigation on shear failure behavior of rock-like samples containing multiple non-persistent joints. *Rock Mech Rock Eng* 53:4717–4744
- Zhang K, Liu X, Liu W, Zhang S (2021) Influence of weak inclusions on the fracturing and fractal behavior of a jointed rock mass containing an opening: experimental and numerical studies. *Comput Geotech* 132:104011
- Zhang T, Liu B, Wei Z, Jiao Z, Song Z, Zhang H (2022) Dynamic mechanical responses and crack evolution of burst-prone coal with a single prefabricated fissure. *Theor Appl Fract Mech* 121:103494
- Zhao K, Yu X, Zhou Y, Wang Q, Wang J, Hao J (2020) Energy evolution of brittle granite under different loading rates. *Int J Rock Mech Min Sci* 132:104392
- Zhou J, Li X, Mitri H (2018) Evaluation method of rockburst: state-of-the-art literature review. *Tunn Undergr Space Technol* 81:632–659
- Zhou Z, Cai X, Li X, Cao W, Du X (2020) Dynamic response and energy evolution of sandstone under coupled static-dynamic compression: insights from experimental study into deep rock engineering applications. *Rock Mech Rock Eng* 53:1305–1331
- Zhu Q, Li D, Han Z, Li X, Zhou Z (2019) Mechanical properties and fracture evolution of sandstone specimens containing different inclusions under uniaxial compression. *Int J Rock Mech Min Sci* 115:33–47
- Zhu Q, Li C, Li X, Li D, Wang W, Chen J (2022) Fracture mechanism and energy evolution of sandstone with a circular inclusion. *Int J Rock Mech Min Sci* 155:105139
- Zhu M, Xie G, Liu L, Wang R, Ruan S, Yang P, Fang Z (2023) Strengthening mechanism of granulated blast-furnace slag on the uniaxial compressive strength of modified magnesium slag-based cemented backfilling material. *Process Saf Environ* 174:722–733

Publisher's Note Springer Nature remains neutral with regard to jurisdictional claims in published maps and institutional affiliations.

Springer Nature or its licensor (e.g. a society or other partner) holds exclusive rights to this article under a publishing agreement with the author(s) or other rightsholder(s); author self-archiving of the accepted manuscript version of this article is solely governed by the terms of such publishing agreement and applicable law.